

Physical processes regulating the seasonal and interannual variability in chlorophyll across the equatorial and North Indian Oceans

Y. Xu¹, Y. Wu¹, H. W. Wang², J. Zhang¹

¹ State Key Laboratory of Estuarine and Coastal Research, East China Normal University, 500 Dongchuan Road, Shanghai, China, 200241.

² Center for Ocean and Climate Research, First Institute of Oceanography, Ministry of Natural Resources, NO.6 Xianxialing Road, Laoshan District, Qingdao, China, 26606.

Corresponding author: Yi Xu (xuyi@sklec.ecnu.edu.cn)

Key Points:

- A newly developed method based on satellite Chl is used to derive vertical Chl distributions in the equatorial and North Indian Oceans.
- Based on a 16-year analysis, seasonal and interannual variability in Chl exist under different driving forcings.
- The Indian Ocean dipole locally and remotely regulates the interannual anomalies of physics and the vertical distribution of Chl.

Abstract

Based on 16-year MODIS-Aqua (MODISA) satellite products, a new method is used to derive vertical Chl distributions in the equatorial and North Indian Oceans. The Chl seasonal and interannual variabilities are examined. The Bay of Bengal (BoB) experiences summer surface Chl (SChl) increases in the areas south and east of Sri Lanka, and SChl increases in the southwestern bay during the winter monsoon. The SChl high in the Sri Lanka Dome (SLD) exists as an annual feature along the time series. Seasonal SChl variance is characterized by a distinct vertical evolution of the mixed layer depth (MLD), with the SChl increase appearing with a shallow MLD in the SLD, while SChl increase with MLD deepens in the southwestern bay in winter. The less productive southern equatorial region explains most of the interannual anomalies with dipole structures present in both the physical fields and Chl. We observed a close correlation between the Indian Ocean dipole (IOD) and the physical field anomalies, such that the wind stress curl is positively correlated with IOD in the eastern equatorial India Ocean and negatively correlated in the south, with the opposite pattern observed in sea surface height (SSH) with IOD. Both surface and subsurface Chl anomalies are closely related to IOD, suggesting the bottom-up transition of thermocline feedback to biology under the remote and local influence of IOD. The advent of depth-resolved satellite Chl improves the understanding of the Chl response to changes in the environment under potential climatic feedbacks in the North Indian Ocean.

Plain Language Summary

The North Indian Ocean experiences semiannual reversal of the monsoon wind across the entire basin north of 10°S, and no climatological upwelling occurs in the eastern equatorial region. This phenomenon makes this region unique, especially when a dipole mode (IOD) exists and influences both the atmosphere and ocean in this region. In this study, based on satellite-derived chlorophyll (Chl) and other independent satellite and in situ match-up data, we examined the seasonal and interannual variabilities in Chl over a 16-year period (2003-2018). We find that significant seasonal variability takes place in the Bay of Bengal (BoB), showing Chl enhancement during the summer monsoon in the area south near Sri Lanka and in the southwestern part of the bay during the winter monsoon. The less productive equatorial and southern regions display interannual variability with east-west oscillations in physical fields and Chl during IOD events. Our analysis also indicates that there are couples/decouples of physics with climatological conditions under negative/positive IODs, which result in different magnitude changes in biology. The analysis of vertical Chl variability suggests different mechanisms of nutrient entrainment, which are driven by the combination of monsoon winds and IOD-induced remote forcings.

1 Introduction

Physical forcings that drive the spatial and temporal variabilities in marine primary productivity in the open ocean have undergone various discussions, with the traditional conceptualization that vertical mixing controls nutrient and light availability (Sverdrup, 1953) as well as adjusting the physiological pressure within phytoplankton communities (Behrenfeld, 2006; Falkowski & Oliver, 2007). In the subtropical/tropical ocean, there is no deep mixing, wind-driven surface flow, coastal upwelling, and open ocean eddies act as the main processes that affect the nutrient supply to the oligotrophic euphotic zone and subsequently trigger surface phytoplankton blooms (Chavez et al., 2011). Climate variability can also drive pronounced changes in phytoplankton primary production in these regions, which has been the focus of many studies, including analyses of long-time in situ time series and satellite chlorophyll a (Chl) (Karl et al., 1996; Gregg & Watson, 2003; Behrenfeld,

2006). Similar to other subtropical/tropical oceans that are well known for their coupled ocean-atmosphere processes, the North Indian Ocean (north of 15°S) differs from the Atlantic and Pacific in a number of climatically important ways. The North Indian Ocean is the only tropical ocean where the annual mean winds on the equator are westerlies, and it is the only ocean basin that is bounded to the north by a continent (i.e., Tibetan Plateau). There are two distinctive features of the weather system in the tropical Indian Ocean: winds generally blow from the southwest during the summer monsoon (June-September) and from the northeast during the winter monsoon (November-February). These biannual reversal of winds force seasonal variations in circulation (Schott & McCreary, 2001) and make a basin-wide unique seasonal characters of phytoplankton bloom in the Indian Ocean (Lévy et al., 2007) that are different with the subtropical North Atlantic, which has traditionally been viewed as a system with annual winter bloom that are driven by seasonal destratification accompanied by nutrient entrainment from depth (Gruber et al., 2002), and different with the oligotrophic subtropical North Pacific which is characterized by strong stratification, chronic nutrient depletion and low Chl.

In the northeastern part of the Indian Ocean, the Bay of Bengal (BoB) is highly forced by monsoons and characterized by low biological productivity compared with its western counterpart, the Arabian Sea. The weak vertical mixing due to freshwater-induced stratification and weak winds have been suggested as the major contributions to the less productivity (Kumar et al., 2002; Vinayachandran et al., 2002). The seasonal variations in the circulation in the BoB and the associated thermocline structure have influenced the biology. Increased Chl in the waters around Sri Lanka was found during the summer monsoon and was associated with a nutrient introduction into the upper layer by coastal upwelling. During the winter monsoon, the positive wind stress curl associated open ocean Ekman pumping has been related to phytoplankton blooms in the southwestern part of the bay (Vinayachandran & Mathew, 2003). Another dominant feature in this region is a cyclonic gyre known as the Sri Lanka Dome (SLD), which is driven by open ocean Ekman pumping and contributes to high Chl concentrations in eastern Sri Lanka (Vinayachandran & Yamagata, 1998; Thushara et al., 2019).

The monsoons also influence the equatorial Indian Ocean regions, making them different from other equatorial oceans. Notably, semiannual eastward winds occur over the equator during intermonsoons, which result in the remarkable Indian Ocean phenomenon of strong eastward surface jets during these periods, commonly referred to as Wyrtki Jets (WJs, Wyrtki, 1973), with maximum speed occurring between 65-85°E. These jets carry warm upper layer waters eastward, causing convergence with downwelling in the east, thereby increasing sea level and mixed layer thickness in the east and decreasing them in the west (Joseph et al., 2012). Although the WJs are an eastward transport phenomenon that occur in the equatorial region, when they are reflected from the eastern boundary in the form of coastal Kelvin and Rossby waves, their impacts can extend to regions away from the equator, i.e., the upwelling regime off Sumatra (Schott et al., 2009). Due to the lack of steady equatorial easterlies, there is no equatorial climatology upwelling in the eastern Indian Ocean; only when there are anomalous easterlies, WJs weaken, and surface divergence shoals the thermocline, the upwelling exists.

Beyond the monsoonal feature in the North Indian Ocean, the Indian Ocean has exhibited its own mode of interannual variability, known as the Indian Ocean dipole (IOD) (Saji et al., 1999; Webster et al., 1999), with associated forcing variabilities that can locally and remotely influence the basin. The positive IOD is associated with anomalous easterly winds on the

equator, weak WJs, a shallow thermocline in the east, and cold SST anomalies off the southwest coast of Sumatra and Java. The opposite anomalies occur over similar regions in the negative IOD phase. The response to IOD is not only confined to the equatorial ocean but also found in other parts of the tropical Indian Ocean. The annual eastward equatorial Kelvin waves, when reflected from the eastern boundary, propagate along the coastal wave guide of the BoB as a coastal Kelvin wave (Rao et al., 2002). During a positive IOD event, an upwelling Kelvin wave propagates along the periphery of the BoB, resulting in an anticyclonic anomalous circulation, which opposes the disintegrated circulation that is normally observed during this season. Conversely, during a negative phase of the IOD, the winter climatological cyclonic circulation pattern is enhanced (Rao et al., 2002). The sea level signals driven by the equatorial wind can also propagate as westward radiating Rossby waves (McCreary et al., 1993). The IOD effects are observed in the way that the downwelling favorable Rossby waves reflected from the eastern boundary propagate to the west and influence the off-equatorial region ($\sim 10^\circ\text{S}$) in the subsurface (Rao et al., 2002; Rao & Behera, 2005).

Under this climatically complex physical framework with both local and remote forcings, a pronounced basin-wide spatiotemporal variability in the physical factors affecting productivity has been explored in terms of the compensating responses among different regions in the Indian Ocean basin. Satellite and in situ observations reveal the presence of intense regional Chl increases and inorganic carbon system variability in the eastern equatorial Indian Ocean (Xue et al., 2014; Ma et al., 2015). Previous studies have examined the physical processes that make the BoB a less productive region than the Arabian Sea (Kumar et al., 2002; Patra et al., 2007). Studies have also focused on a particular case of pronounced IOD and ENSO events (i.e., 1997/1998 IOD and ENSO): Based on SeaWiFS Chl, basin-wide net primary production (NPP) anomalies were used to assess the impact of IOD/El Niño events on biogeochemical processes, with positive NPP and Chl anomalies both shown in the eastern Indian Ocean during IOD events and more extensive NPP distributions when negative anomalies occur (Wiggert et al., 2009); A coupled biogeochemical model combined with SeaWiFS Chl was used to investigate changes in Chl both at the surface and subsurface caused by the 1997/1998 IOD and ENSO events in the Indian Ocean (Currie et al., 2013). Based on SeaWiFS Chl, the phytoplankton size structure in the Indian Ocean was examined under the influence of IOD (Brewin et al., 2012).

The purpose of this paper is to obtain a complete picture of the Chl variability in the North Indian Ocean and the equatorial region (bounded east of 78°E and north of 15°S) from 2003-2018, with a focus on increasing the understanding of the monsoon and climate oscillation-regulated seasonal and interannual variabilities in Chl using observations with sufficient spatial and temporal coverage. In particular, we aim to examine the vertical evolution of Chl variability and the underlying physical mechanisms. The independent data sets used are presented in section 2. In section 3, the spatial and temporal variability in surface chlorophyll (SChl) and vertical Chl will be investigated under the framework of coupled seasonal monsoon and equatorial climate signals that have modulated this region with remarkable physical phenomena. Then, biota zones will be identified based on the empirical orthogonal function (EOF) results, with the vertical Chl evolution in each zone being individually examined. Finally, the interannual variability in this region will be assessed by checking the leading mode of the EOF analysis applied to physical and biological field anomalies, and an irregular oscillation will be examined with IOD. The mechanisms driving these fluctuations will also be discussed. The summary and discussion of our results are presented in section 4.

2 Materials and Methods

We use the fully developed Carbon-based Production Model (CbPM) (Behrenfeld et al. 2005; Westberry et al. 2008) to obtain vertical profiles of Chl. This model is a new approach based on satellite products, including information on the subsurface light field and nitracline depths to parameterize photoacclimation and nutrient stress in phytoplankton physiology throughout the water column. All the input data used for mode calculation were downloaded from <http://www.science.oregonstate.edu>, with a spatial resolution of ~9 km, and temporal scale from 2003/01-2018/12, including MODISA-derived monthly Chl and backscatter (BBP), which are based on the GSM algorithms, and diffuse attenuation at 490 nm ($K_d(490)$), photosynthetically available radiation (PAR), and SST, which are based on MODIS.r2018 reprocessing results. The mixed layer depth (MLD) is provided by the HYbrid Coordinate Ocean Model (HYCOM) output of the global model GLBu0.08 hindcast and is defined as a 0.5 degree decrease in temperature from the value at the surface. Climatological values of 1° resolution WOA18 nitrate data are used for the nitracline estimate. The bottom of the nitrate-depleted surface layer (referred to in the following as “nitracline”) is defined as the depth where the nitrate concentration exceeds 0.5 μM (<https://www.nodc.noaa.gov/OC5/woa18/>). The euphotic depth was computed following 1% of surface PAR.

By using the CbPM model, the vertical profiles of Chl are evaluated by considering the light and nutrient change-induced pigment adjustment with depth. Chl changes as a function of light, nutrient, and MLD. The light is attenuated due to Chl and other visible spectra in the water column. Within the mixed layer, all properties (except light) are assumed to be homogeneous, and phytoplankton are assumed to be acclimated to median PAR in the mixed layer. Below the mixed layer, the phytoplankton community photoacclimates to a lower light level, thus changing the Chl biomass, which in turn changes the spectral attenuation accordingly. When the MLD approaches the nitracline, the nutrient stress for phytoplankton blooms reaches zero, and an increase in Chl occurs at the bottom of the mixed layer, indicating the combined effects of photoacclimation and decreasing nutrient stress. Further below, the light continues to decrease, and there is a more gradual increase in Chl due to photoacclimation until the phytoplankton growth rate becomes less than the background loss rate. Then, Chl starts to decrease and gives rise to a subsurface Chl maximum layer. Below the subsurface Chl maximum layer, the light, as well as the phytoplankton growth rate and Chl, continue to decrease. The CbPM model-derived vertical distribution of Chl was compared with the chlorophyll fluorescence measured based on the cruise track conducted in April 2013 along 88°E (supplementary information). The model is able to reproduce the surface Chl maximum layer at approximately 50~80 m and matches the latitudinal distribution of Chl from the observations.

As a comparison with other physical variables with different measurement sources, we produced wind, net heat flux (NHF), and sea surface height (SSH) for the same periods. Wind data are from the European Centre for Medium-Range Weather Forecasts (ECMWF), ERA-Interim, which is a global atmospheric reanalysis that is available at <https://www.ecmwf.int/en/forecasts/datasets/reanalysis-datasets/>. The local surface wind stress curl ($\nabla \times \tau$, $\partial\tau_y/\partial x - \partial\tau_x/\partial y$, with x and y as the eastward and northward coordinates, respectively, and τ_x , τ_y are the corresponding components of the surface stress) was calculated based on monthly wind generated from ERA-Interim hourly data. In addition

to the local wind stress curl, we consider air-sea fluxes from the ECMWF reanalysis. The NHF is derived from the shortwave and longwave radiation and sensible and latent heat fluxes. Monthly mean multimission gridded satellite products of SSH were downloaded from the Archiving, Validation and Interpretation of Satellite Oceanographic Data website (AVISO, <http://www.aviso.oceanobs.com/>) for the same periods as MODISA Chl.

To calculate the anomalies, monthly climatologies for SSH, wind, and Chl were first produced for the 16-year period on a pixel-by-pixel basis, and then, the monthly climatologies were moved by subtracting each monthly climatology from the corresponding month of the time series to obtain the anomalies.

3 Results

3.1 EOF analysis of SChl

EOF analysis partitions the SChl covariance among locations into a series of orthogonal modes, each having a spatial pattern that is associated with a time series of variability in that mode. Sixteen years of MODISA-derived monthly SChl composites were used to investigate the spatial and temporal variability in surface phytoplankton productivity in this region. The first mode (33% of the total variance) shows variability of the seasonal pattern with maxima from June to September during the summer monsoon in the temporal amplitude (Figure 1e). The spatial loadings are almost positive, and in phase in the whole domain. It shows high positive loadings along the east coast of India with the most significant positive variabilities in the areas west and south of Sri Lanka (Figure 1a). This feature is associated with coastal upwelling driven by southwest monsoon winds that cause nutrient enrichment to the surface layer in these regions (Vinayachandran et al., 2004). The southwest monsoon current also advects Chl-rich India/Sri Lanka coastal waters into the bay along its path, as shown in the EOF spatial loadings, where a high Chl band was found extending eastward from the southeastern tip of Sri Lanka. High EOF loadings seen east of Sri Lanka are completely separated from the coast, corresponding with a cyclonic eddy known as the SLD, which usually matures east of Sri Lanka in June, as noted previously by Vinayachandran & Yamagata (1998) and Burns et al. (2017).

The seasonal climatology of the physical background wind and SSH field were analyzed to establish a link with the SChl variability (Figure 2). Biannual reversing monsoon winds dominate the BoB and result in a unique seasonal dependence of the wind stress curl. Anticyclonic surface wind stress curl dominant in the intermonsoonal months (February–April) and generate an anticyclonic current gyre (Shetye et al. 1993) with anomalously high SSH in the western bay due to convergence (Figure 2b–d). The gyre disappears during the southwest monsoon when positive wind stress curl occur in the northeast corner of Sri Lanka, and then, the wind turns southwest in June, which shapes a negative SSH anomaly (Figure 2f) and corresponds with high SChl in EOF mode 1.

The second mode accounts for approximately 14% of the total variance. As shown by the related spatial loadings (Figure 1b), the high positive loadings are in the western BoB along the east coast of India, where a well-known monsoon-driven regional dynamic exists. Temporal variabilities show high coefficients during the northeast monsoon (November–February), with the highest coefficients in December. When times the positive spatial variabilities, indicate high SChl the western BoB during this period. The positive wind stress curl starts to dominate the southwest BoB with the transition of the southwest monsoon to the northwest and leads to anomalously low SSH during October to January in the southwest of

the Bay (Figure 2j, k, l, and a). The winter time SchI high detected in this mode is consistent with results of previous studies in this region that northeasterly winds driven open Ekman pumping upwells nutrient and sustain phytoplankton blooms (Vinayachandran & Mathew, 2003).

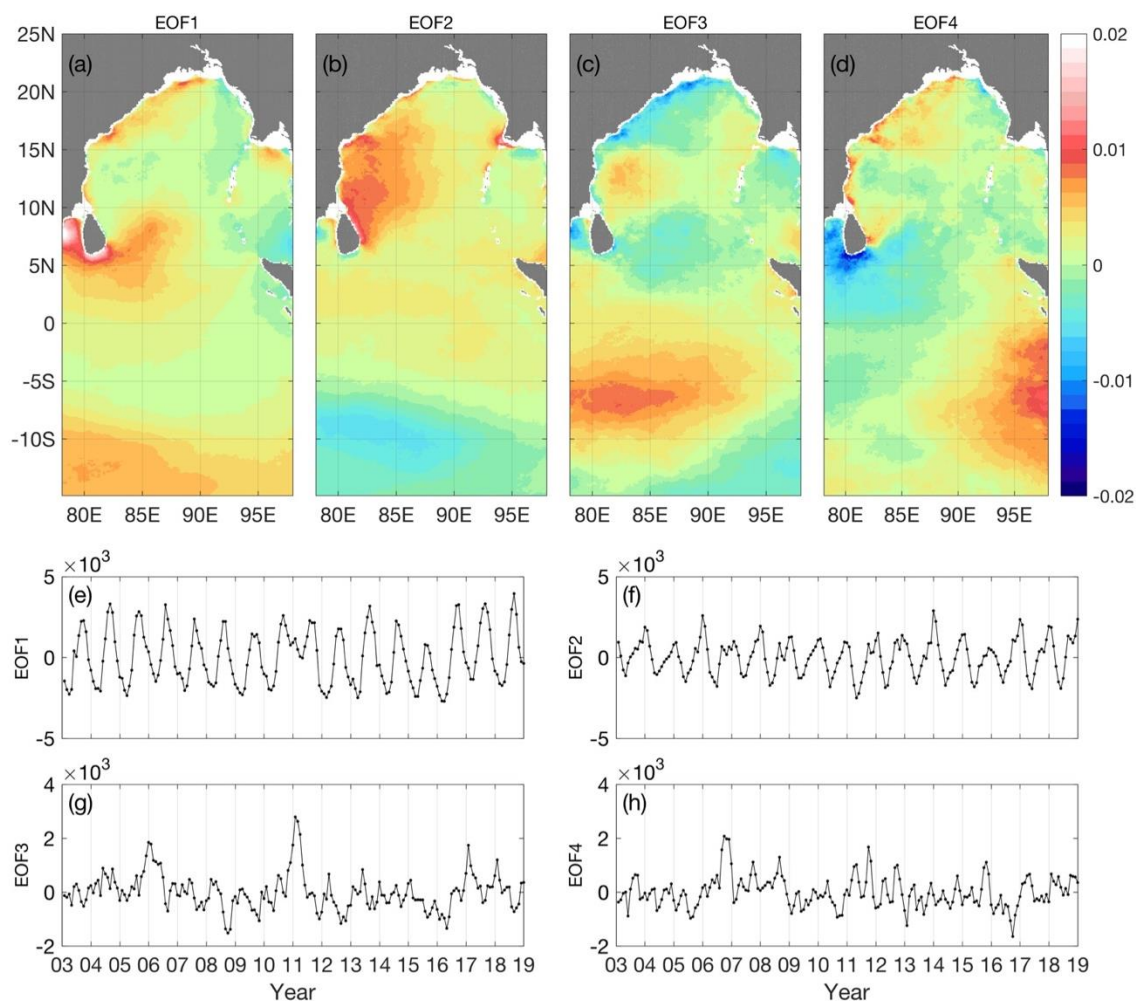


Figure 1. Leading modes of EOF results for SchI. Upper panels show the spatial structures of the first four modes (a)-(d). The temporal amplitudes for the four modes are shown in (e)-(h).

The third EOF mode accounts for approximately 5% of the total variance. The spatial distributions of this mode are related to significant SchI variability in the open ocean between 5-10°S (Figure 1c), where a shallow thermocline area have been confined in the same place, and with prominent SST variance. Positive wind stress curls are identified throughout the year along the equator to the south with largest value showing between 5-10°S during boreal fall-winter in the seasonal climatology field (Figure 2j-l). In the same region identified in Chl EOF mode 3, where the southeasterly trades in the southern Indian Ocean meet the equatorial westerlies, positive curl form (Schott & McCreary, 2001), drive the cyclonic equatorial gyre and result in upwelling and enhanced SchI. As shown in the temporal amplitude (Figure 1g), a pronounced high SchI in this region exists during the boreal winters of 2005-2006, 2010-2011, and 2015-2016 (Figure 1g). Although this open ocean upwelling zone exists year round in the central south Indian Ocean, it is relatively weak, and its effect is masked by an equatorward SST gradient (Xie et al., 2002). Therefore, the anomalies in the east could also radiate to the interannual variability in this region.

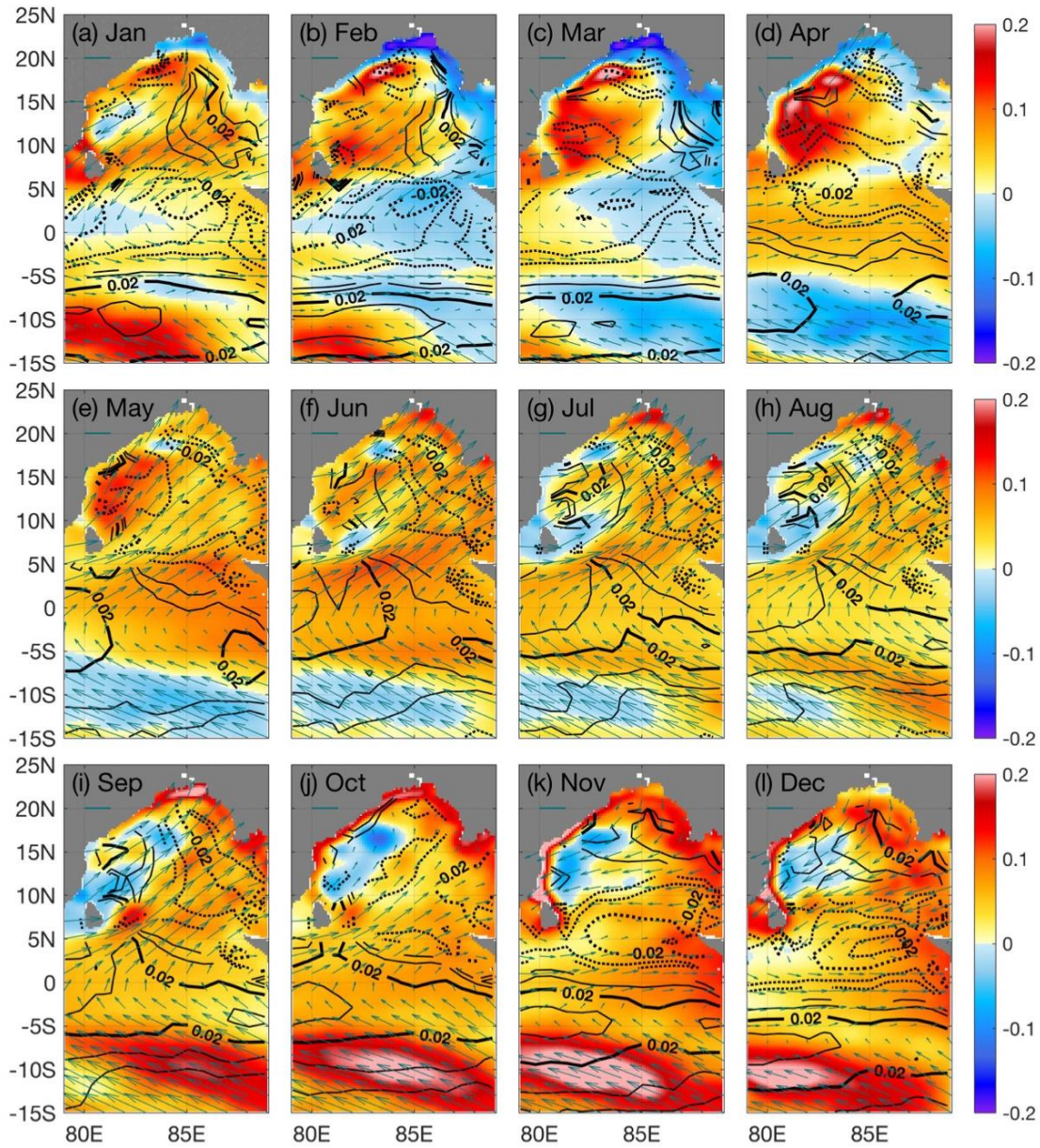


Figure 2. Seasonal climatology of SSH anomalies (color; m), wind stress curl (contour lines; 10^{-6} N m^{-3}), and wind vectors (scale factor is 5 m s^{-1}).

The fourth EOF mode (approximately 4% of the total variance) shows negative loadings over the western part of the study area with the lowest loadings found in area south of Sri Lanka, and positive loadings over the eastern part of the study area with the highest loadings at approximately 55°S in the tropical eastern Indian Ocean near the coast of Sumatra (Figure 1d). This mode indicates an oscillation between the eastern and western regions, which has been demonstrated in previous analyses of the SSH and SST fields (Rao et al., 2002; Huang et al., 2002). Combined with the temporal amplitude, the increase in SCHl that persisted throughout the eastern equatorial Indian Ocean and southward to the coastline of Sumatra is most pronounced in September-December of 2006 and 2015, while the decrease in SCHl occurred south of Sri Lanka during the same time. Opposing variabilities take place in fall

2010 and 2016, as shown in the temporal pattern. Mechanisms contributing to the interannual anomalies are examined in the following section.

3.2 Biota zones

To further identify the zones with characteristic variabilities, we extend the EOF analysis results in section 3.1 by calculating the percentage of the local variance explained by the first four EOF modes. Four biota zones in our study area are identified, each of which can explain more than 50% of the local variance (Figure 3a). The monthly climatology of the spatial mean SCHl, NHF and SST in the four zones are shown in Figure 3b-c. This figure highlights the seasonality variance in these regions in terms of timing and magnitude.

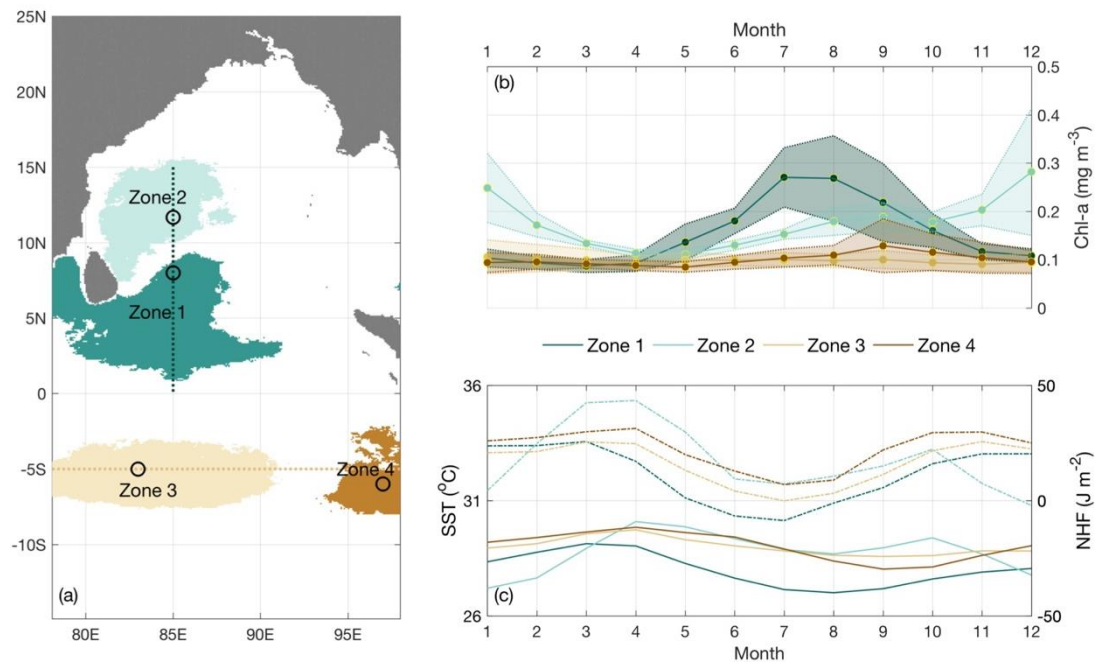


Figure 3. (a) Four biota zones identified by the EOF analysis. (b) Seasonal climatology of spatial mean SCHl in the four biota zones. (c) Seasonal climatology of spatial mean SST (solid line) and NHF (dashed line) in the four biota zones.

In the area south of Sri Lanka (zone 1), SCHl starts to increase in May with the onset of the summer monsoon, reaching a maximum in July/August as the monsoon reaches its strongest (Figure 3b). SST is lowest during the summer monsoon periods, which is the same as the NHF seasonality (Figure 3c). The decrease in NHF during the summer monsoon season is associated with monsoon-induced precipitation that can cover 65% of the total rainfall in a year (Weller et al., 2019), and accompanied by a decrease in solar radiation due to cloud cover. In the southwestern part of the BoB (zone 2), SCHl is high during winter monsoons (December-January). This winter bloom occurs in response to convective vertical mixing driven by cold, dry northeasterly winds. The maximum NHF exists during the inter-monsoon periods with higher SST during March/April than in October. Cloud free and light winds contribute to the strongest ocean heating. After the NHF peaks in the spring during the inter-monsoon, the NHF starts to decrease and remains low during the summer monsoon, which is mostly due to the heat loss during the latent flux exchange (not shown here). The maximum NHF loss occurs in December, the month when the SCHl peaks. This suggests that superposition of wind mixing and northeast monsoon-induced open ocean Ekman pumping

maximizes the amount of phytoplankton blooms in this region. The SST in zone 2 indicates a clear semiannual cycle characterized by higher SSTs during March/April and October and a minimum SST during the winter monsoon. The in-phase variabilities between SST and NHF indicate the occurrence of oceanic-atmospheric feedback. The SChl values in zone 3 and zone 4 are much lower than those in zone 1 and zone 2 and have less seasonal variability. The seasonal climatologies of SST and NHF in zone 3 and zone 4 are similar to those in zone 1, with lowest NHF in the summer and higher NHF during the inter-monsoon seasons; however, they show higher values which are in response to lower wind mixing near the equatorial south region.

To further explore the vertical Chl variability in the four biotas identified in our study area, sections along 85°E and 5°S are chosen to examine the longitude- or latitude-associated dominant vertical features. Surface phytoplankton production is modulated by fluxes in nutrient through the base of the mixed layer and the availability of light. Nutrient are initially exhausted at the surface, and the bloom can be triggered by the supply of nutrient due to upwelling, convection, or horizontal advection. To check the vertical evolution of Chl, a single pixel in each zone (indicated in Figure 3a) representing different water properties was chosen to present the variabilities in Chl, MLD, and Z_{eu} in the upper 200 m along the time series.

a. Bay of Bengal region

The grid in zone 1 that represents the SLD-modulated feature is selected to examine the vertical evolution of Chl along the time series (Figure 4a). The euphotic zone depth is deeper than the MLD in all years, suggesting that light is not a limiting factor for phytoplankton growth. A subsurface Chl maximum exists at the bottom of the MLD between 50-75 m, indicating the local maximum in the phytoplankton growth rate near the MLD and photoacclimation of pigment content. Enhanced Chl events on the surface are observed starting in the middle of a year with the deepening of the MLD, and the maximum SChl appears at the time when the MLD is uplifted as the SLD matures. The comparison between the highest SChl time (June) and the lowest SChl time (April) captured the increase in SChl with the uplifted MLD, revealing that the development of phytoplankton blooms in the upper mixed layer is facilitated by the dome (Figure 4c).

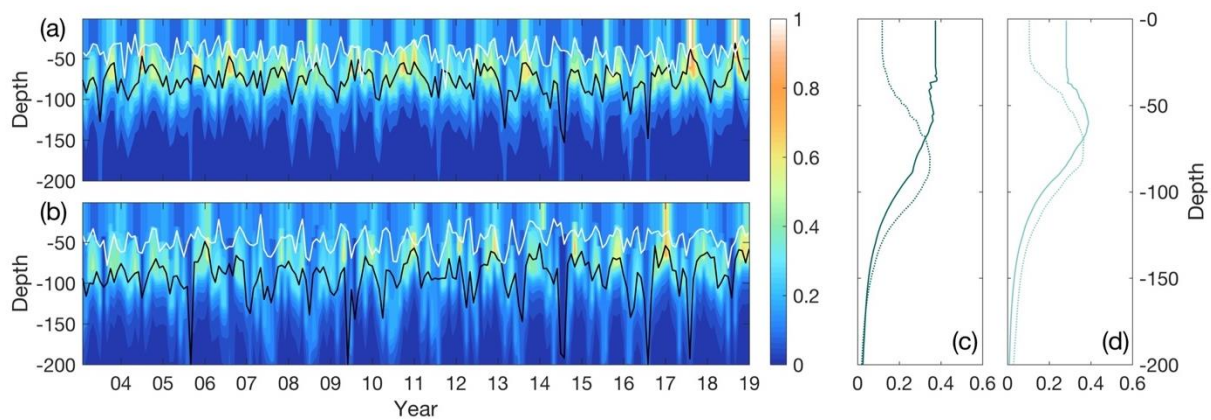


Figure 4. Time series of vertical Chl in biota zone 1 (a) and zone 2 (b). The black lines represent the euphotic zone depth, and the white lines represent the MLD. Right panel: Comparison of two Chl profiles with one at the time when SChl is highest (solid line) and the

other when SCHl is lowest (dashed line). (c) is for the grid in zone 1. (d) is for the grid in zone 2.

The grid in zone 2 located further north along 85°E is shown in Figure 4b. The time series shows a deeper Z_{eu} than the MLD and a notably high Chl between 50-100 m depth. Subsurface Chl starts to increase earlier in fall with shallowing of the MLD. A high SCHl only appears in boreal winter when the MLD is deep enough. The Chl and MLD patterns support the notion that during the northwest monsoon, a cyclonic gyre that occupies in the southwestern bay causes Ekman pumping that lifts the thermocline, transports nutrient from depth and triggers a fall subsurface bloom. The SCHl maximum exists at the time that the thermocline has already been lifted by Ekman pumping, and winter mixing enhances the entrainment of nutrient into the upper mixed layer from the bottom of the deepened mixed layer. The comparison between the highest SCHl time (December) and the lowest SCHl time (April) indicates the deepening of the MLD when the surface Chl reaches its maximum (Figure 4d).

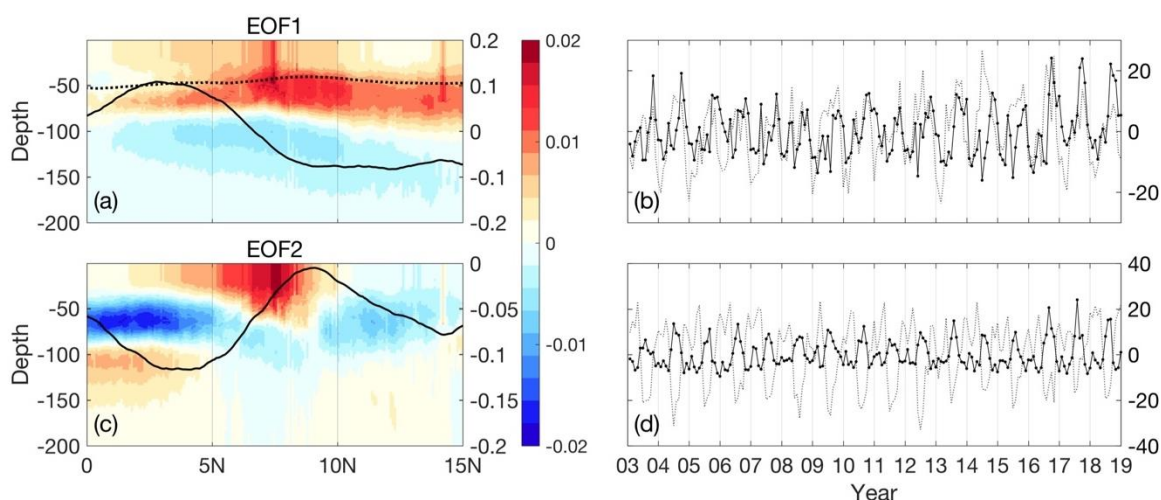


Figure 5. EOF analysis of Chl in the section along 85°E. (a) Spatial structure of the 1st EOF mode. The EOF of the MLD is overlaid (solid black line), and the climatology of the MLD is overlaid as a black dashed line. (b) Temporal amplitudes of Chl (solid line) and MLD (dashed line). (c) Spatial structures of EOF mode 2 for Chl and MLD. (d) Temporal amplitudes of EOF mode 2 of Chl (solid line) and MLD (dashed line).

An EOF analysis of Chl and MLD along 85°E confirmed the different mechanisms of Chl variabilities, as interpreted in the above results. The first EOF mode explains 24% of the total variance and shows the maximum Chl in the subsurface layer with relatively high loadings in the upper mixed layer during boreal fall-winter (Figure 5a, b). This result corresponds with the second MLD EOF mode (22.4% of the total variance) that displays a sloping thermocline generally uplifted from north to south and MLD deepening during boreal fall-winter, as shown in the temporal amplitudes (Figure 5a, black line). The monthly climatology plots of MLD, nitracline and NHF (Figure 6) indicate the decrease of NHF and deepening of MLD occur beginning in October, with shallowing of nitracline depth in the northern part of the section. The NHF became negative in December, indicating destratification due to winter convection. The first EOF mode along 85°E captures the features of nitracline lift and MLD deepening during boreal fall-winter and the associated subsurface and surface Chl high.

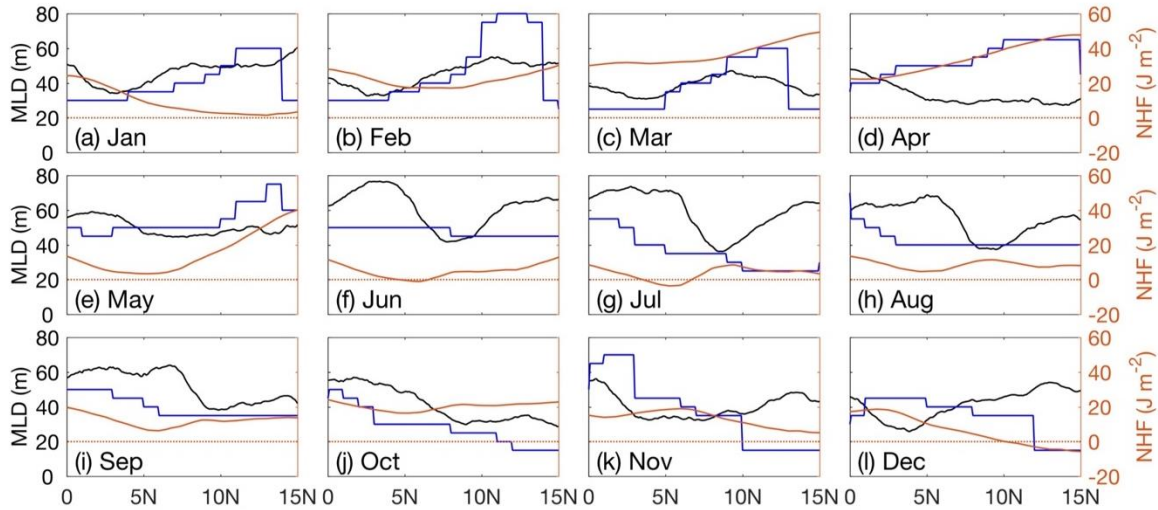


Figure 6. Seasonal climatology of MLD (black), nitracline (blue) and NHF (orange) along the section at 85°E.

The second EOF mode of vertical Chl (13% of the total variance) matches the first EOF mode of MLD (49.7% of the total variance), indicating a dome-shaped vertical loading of high Chl in the upper layer. Maximum Chl EOF loadings were found between 5-9°N. The corresponding temporal amplitude steadily increases beginning in April and reaches a maximum in July/August. This MLD feature represents an uplifted dome shape between 5-9°N (Figure 6f-h, black line), suggesting eddy development around April and intensification in July or August. Under the right divergent conditions, cool, nutrient-rich waters can be upwelled from deeper waters to the surface and result in enhanced SChl. Seasonal nitracline variance indicates that shallowing of nitracline starts in July, with the increase in NHF in the position of the eddy, as illustrated in Figure 6; this finding suggests that eddy-induced pumping of nutrient in the center of the eddy and cold water from the deep surface result in a positive sensible flux into the ocean (Figure 6f-h, orange line). This feature indicates enhanced productivity in the upper mixed layer associated with the SLD (Figure 7), which has been reported to first form in approximately May, mature in July, and decay in approximately September (Burns et al., 2017).

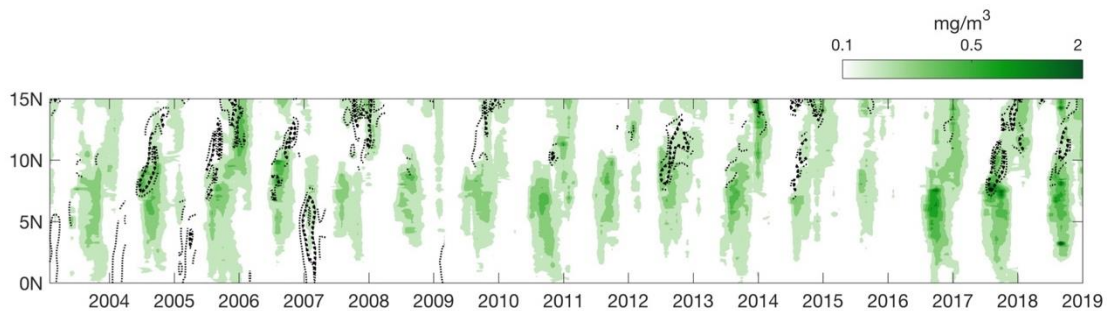


Figure 7. Time series of SChl along 85°E as a function of latitude and year from 2003-2018. SSH anomalies are plotted as black dashed lines (contour interval 0.1 m). The -0.1 contour lines are highlighted as bold dashed lines.

b. Equator south region

The Chl of the grid in zone 3 indicates a significant subsurface Chl maximum along the time series. There is an annual deepening of MLD starting in boreal summer and increasing during fall-winter (Figure 8). Z_{eu} is deeper than the mixed layer most of the time. Less seasonal variability of Chl is found in the upper mixed layer. The grid in zone 4 on the east side indicates the same seasonal pattern of deepened MLD in summer and enhanced MLD in fall-winter; however, the MLD is relatively deeper than the grid in zone 3, which has been detailed in the literature that a west-to-east gradient in the thermocline in this region. The comparisons between the highest SChl time (January for zone 3, September for zone 4) and the lowest SChl time April for zone 3, May for zone 4) indicate the increase of surface Chl with shallowing of MLD for the grids in zone 3 and zone 4 (Figure 8 c, d).

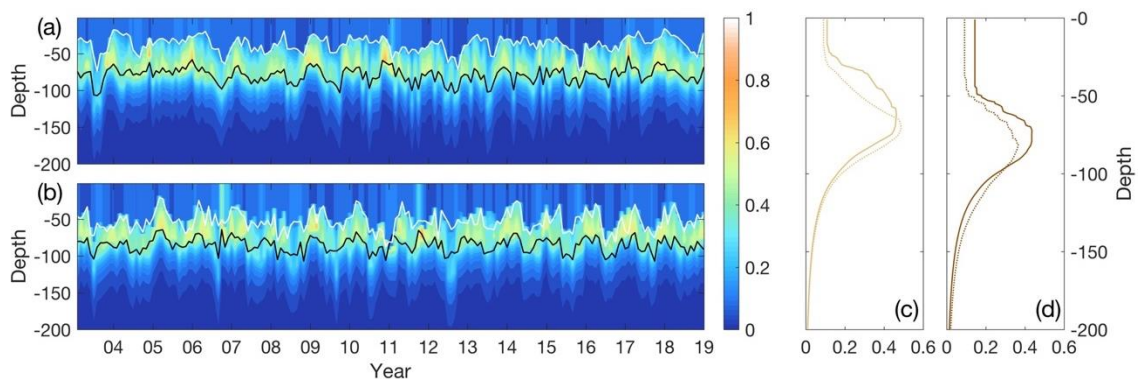


Figure 8. Time series of vertical Chl in biota zone 3 (a) and zone 4 (b). The black lines represent the euphotic zone depth. The white lines represent MLD. Right panel: Comparison of two Chl profiles with one at the time when SChl is highest (solid line) and the other when SChl is lowest (dashed line). (c) is for the grid in zone 3. (d) is for the grid in zone 4.

The EOF analysis of Chl and MLD along 5°S represents a stratified tropical ocean vertical Chl seasonality in the first mode (Figure 9a). The Chl EOF explains 43% of the total variance, which is characterized by longitudinal uniform positive loadings with the highest variance existing between 30-70 m depth, near-zero EOF loadings on the surface, and negative loadings at depth, indicating subsurface Chl maximum and a decline in Chl due to increased light attenuation by phytoplankton in the upper layer. The temporal amplitude increases steadily from July/August and reaches a maximum in December, indicating an increase in Chl during these periods. The first EOF of MLD (explains 57.7% of the total variance) indicates a dome shape with maximum variability occurring at the same longitude where Chl EOF loadings are at the maximum (between $85\text{--}92^{\circ}\text{E}$) and similar temporal variability with Chl (Figure 9b, gray dashed line). The relationship between Chl and MLD suggests that the positive temporal amplitude during fall-winter indicates an increase in subsurface Chl and shallowing of MLD at that time, and the reverse variability takes place in summer. This result is consistent with the interpretation from MLD and nitracline seasonal climatology (Figure 10), where there is significant shallowing of MLD starting in October. One month later, the nitracline lifts to ~ 30 m and is shallower than the MLD, especially in the western part of the section (Figure 10), suggesting that the increase in Chl was triggered by shallowing of MLD and nutrient intrusion into the upper mixed layer. Seasonal MLD deepening starts in June and occurs until August (negative MLD EOF temporal amplitude, Figure 9b, gray dashed line) along with a decrease in NHF in response to the northward migration of the sun and atmospheric deep convection (Figure 10f-h). When combining the EOF features of Chl and MLD, the results suggest that the intensification of the subsurface

Chl maximum can be related to the shallowing of the thermocline such that the vertical transport of nutrient is affected by changes in thermocline depth. Based on further interpretation of the underlying mechanism, we found that a positive wind stress curl occurs beginning in boreal fall and peaks in winter over this area (Figure 2j-l), suggesting that Ekman pumping uplifts the thermocline and induces enhanced subsurface Chl.

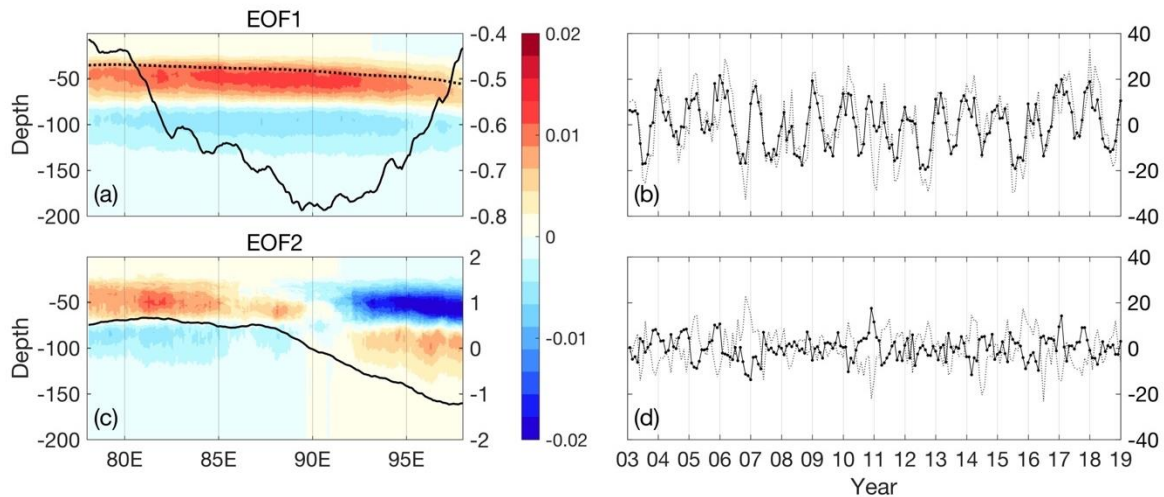


Figure 9. EOF analysis of Chl in the section along 5°S. (a) Spatial structure of the 1st EOF mode. The EOF of the MLD is overlaid (solid black line), and the climatology of the MLD is overlain as a black dashed line. (b) Temporal amplitudes of Chl (solid line) and MLD (dashed line). (c) Spatial structures of EOF mode 2 for Chl and MLD. (d) Temporal amplitudes of EOF mode 2 of Chl (solid line) and MLD (dashed line).

The second Chl EOF characterizes the signal of interannual variability in the subsurface (9.4% of the total variance). This mode exhibits zero loadings crossing near 90°E with inverse variability on the west and east sides (Figure 9c). On the west side, there are positive loadings, indicating an increase in Chl in the upper layer when the temporal amplitudes are positive (i.e., in boreal fall-winter of 2005 and 2010), which is in contrast to the decrease in Chl in the eastern area at the same time. The negative loadings east of 90°E represent an increase in Chl in the negative temporal amplitude and a decrease in Chl at the same time in the west (in boreal winter of 2006-2007). This finding agrees with the third mode of EOF analysis of SChl, as indicated in Figure 1c and g. A pronounced increase in SChl is found in the boreal fall-winter of 2005 and 2010 in this region. This finding suggests that strong Ekman pumping could influence from the subsurface up to the surface, leading to Chl interannual variabilities as presented in our EOF mode.

Similarly, MLD EOF mode 2 is characterized by contrasting variabilities in the east and west, with stronger variance in the east than in the west. Along the time series, the temporal amplitude shows a negative correlation with Chl temporal amplitude, suggesting a pattern of MLD shallowing with an increase in Chl on the east side and MLD deepening in response to a decrease in Chl on the west side. The subsurface Chl east-west oscillation reveals the same information from the MLD variation, indicating coupled physical-biological interactions. The MLD seasonal climatology shows a deeper MLD in the east that could be associated with slightly cooler waters in the western tropical Indian Ocean, causing a west-to-east gradient in the thermocline. A barrier layer in the eastern equatorial Indian Ocean due to large precipitation (Kumar & Prasad, 1997) could also contribute to the deepening of the MLD in the east. In the west, a year-round upwelling zone presents from 5-15°S and 50-80°E due to

wind curl driving the uplifted thermocline in the west (Schott & McCreary, 2001). Beyond the seasonal climatology of the west-to-east thermocline gradient condition, and the pronounced oscillation of MLD in certain years indicates that the fluctuations induced by the interannual ocean dynamics could induce subsurface and surface variability in biology.

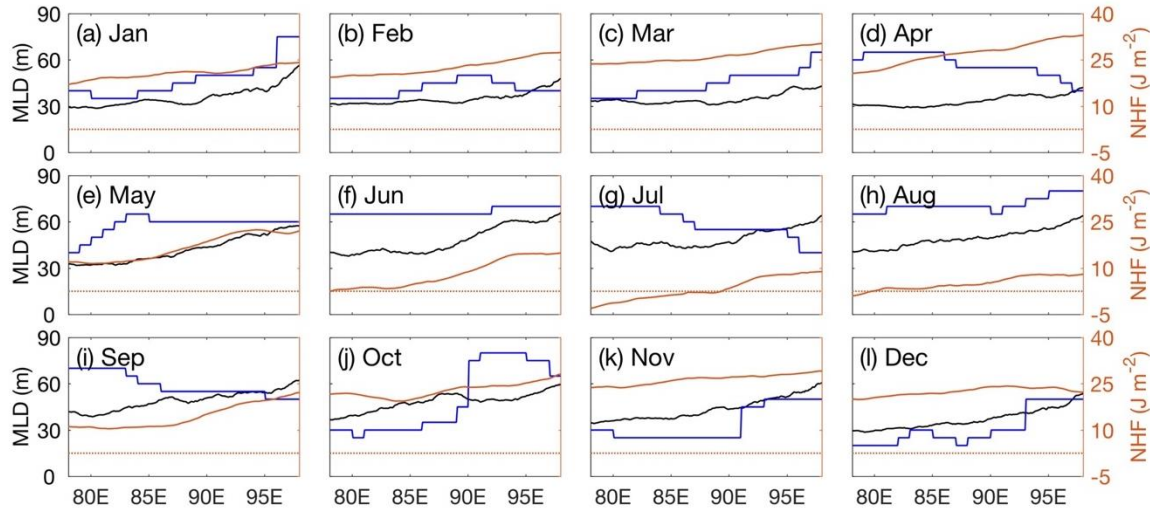


Figure 10. Seasonal climatology of MLD (black), nitracline (blue) and NHF (orange) along the section at 5°S.

3.3 Leading Mode of Interannual Variability

Through the EOF analysis of Chl, a substantial fraction of the temporal variability occurs at annual and shorter periods in the first mode. To focus on interannual scales, we first remove the seasonal cycle from the time series by subtracting the seasonal climatology of each month in each pixel. Then, we analyzed the anomalous variabilities in physical and biological components (wind, SSH, and Chl) using the EOF analysis. By doing so, we could identify when and where the anomalous increase/decrease in the components takes place. Different from the EOF analysis in section 3.1, the EOF analysis in this section can capture the interannual signal in the leading mode and provide a direct comparison of the physical and biological components that are coupled in the system. In the upper panel of Figure 11, the EOF spatial structures of the first mode (EOF1) for all components are shown as color maps. In the lower panel of Figure 11, the temporal amplitudes are normalized by the maximum and plotted with DMI (IOD index, where DMI is defined as the SSTa difference between the western node (10°S-10°N, 50-70°E) and eastern node (10°S-0°, 90-110°E) regions (Saji et al., 1999) and were downloaded from the Japanese Agency for Marine-Earth Science and Technology (JAMSTEC), <http://www.jamstec.go.jp/frsgc/research/>). A positive DMI value indicates an IOD event, and vice versa. To link the dominant mode of physics and biology with the Indian Ocean's own model of interannual variability, we also calculated the correlation coefficient between each of the EOF temporal amplitudes and DMI.

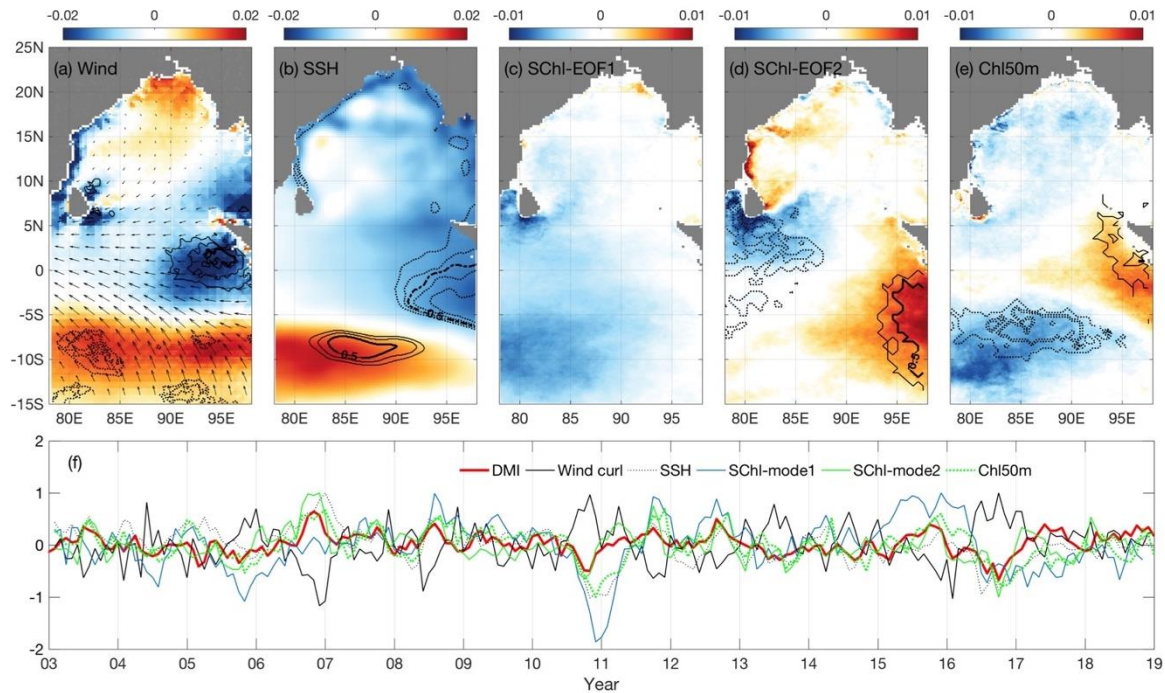


Figure 11. Spatial structure of the first EOF mode of anomalous wind stress curl (a), SSH (b), SCHl (c), and Chl at 50 m (e). The second EOF mode of SCHl is plotted in (d). In (a), the EOF modes of the wind component are shown as vectors. The temporal amplitudes are shown in (f) with the DMI. The contour lines in each of the maps indicate the pixel-by-pixel correlation coefficients (passing the 99% significance level) between the DMI and anomalies, the solid line indicates a positive correlation, and the dashed line indicates a negative correlation.

Figure 11a shows the EOF1 spatial structure of the wind stress curl with spatial loadings of the EOF1 wind vector overlaid. For the wind vector EOF1 (16.7% of the total variance), easterly wind anomalies are identified along the equator with alongshore components near the southeast coast and anomalous southeast winds that are prominent in the central southern ocean. The wind stress curl (13.8% of the total variance) spatial structure is characterized by contrasting negative features on the northern side of 5°S in the eastern equatorial region (Figure 11a, dark blue) and positive features on the southern side, which indicates an oscillation when there is an increase in the wind stress curl in the eastern equatorial region, and correspondingly, a decrease in the wind stress curl emerges in the south. Furthermore, the time series of the first mode shows strong negative peaks occurring during boreal fall-winter of 2006 and 2015, and positive peaks during boreal fall-winter of 2010 and 2016 (Figure 11f, black line), coinciding with the positive IOD and negative IOD events, respectively (correlation significant at the 99% level, $R=-0.51$). Taking the positive IOD in fall 2006 as an example, the negative EOF loadings multiplied by the negative temporal amplitude in fall 2006 indicate an increase in the wind stress curl in fall 2006 in the eastern equatorial region, and conversely, the maximum EOF wind stress curl loadings are found in the southwestern area, revealing that there are anomalously low (decrease) wind stress curls compared with the seasonal climatology at the same time.

The SSH that represents the oceanic response to the surface wind anomalies agrees with what we observe in the wind field. An oscillating pattern of SSH EOF1 is clearly seen in the tropical Indian Ocean with negative loadings in the northeast and positive loadings at the

southern equator (Figure 11b). The associated temporal amplitudes are opposite with the wind stress curl temporal amplitudes (Figure 11 f, black dashed line) but coincide with major IOD events with a significant positive correlation ($R=0.53$, $p<0.01$). The out-of-phase variability in the wind and SSH fields suggests that during a positive IOD, an increase in the positive wind stress curl in the equatorial east induces open ocean Ekman pumping, resulting in negative SSH anomalies (lower SSH), while during a negative IOD, opposite conditions to that of the positive phase prevail.

The SChl EOF1 (16.9% of the total variance, Figure 11c) indicates that negative loadings with a maximum variance appear in the area southwest of Sri Lanka and south of the equator from 5-15°S near 85°E, which is different from the SSH and wind spatial structure of oscillation-type regional positive and negative loadings. The low correlation ($R=0.59$, $p<0.01$) is mostly due to a lag of approximately two months for the SChl EOF model temporal amplitude when compared with the DMI (Figure 11e, blue line). This delay is associated with the reflected Rossby waves spreading the IOD signals from east to west. An oscillating pattern can be seen in the second mode of SChl EOF with positive loadings in the east equatorial region and negative loadings in the areas south and west of Sri Lanka (6.8% of the total variance, Figure 11d). A high correlation was found between the corresponding temporal amplitude and DMI ($R=0.68$, $p<0.01$). The dominant variability captured in the SChl EOF model is the pronounced increase in Chl south of Sri Lanka and a wider region in the southern equator during negative DMI events (i.e., fall 2010), which overwhelm the east-west oscillation shown in the second mode. When applying the EOF analysis on Chl at 50 m (Chl50m), an oscillating feature is present in the first mode, with positive loadings in the east and negative loadings at the southern equator between 5-15°S. The correlation between the DMI and temporal amplitude of Chl50m EOF1 was 0.47 ($p<0.01$) (Figure 11e, green dashed line).

The pixel-by-pixel correlation coefficients between the anomalies and DMI over the 16-year time series are shown as contour lines in the color map. The DMI is positively correlated with the wind stress curl in the eastern equatorial region (Figure 11a, significant at the 99% level, solid contour line) and negatively correlated at the southern equator, with a corresponding opposing relationship found between the DMI and SSH anomaly in the same place (Figure 11a, b black contour lines). The positive correlation between DMI and SChl exists on the east side from the southern equator to 15°S, and a negative correlation is shown on the west side in the area southwest of Sri Lanka (Figure 11c). At a depth of 50 m, there is still a positive correlation in the east further north to 5°S and a negative correlation in the west and equatorial south; however, there is a lower correlation coefficient ($R<0.5$). This finding suggests the remote forcing from the IOD by northwestward propagation of the IOD influences the area from Java to the Sumatra coast, the westward propagation of the downwelling Rossby wave force by the IOD to the south Indian Ocean and deepening of the thermocline in the west (Murtugudde et al., 2000; Chen et al., 2016). This close coupling provides evidence that all the components of a system, including physical and biological, are intrinsically linked under the combined effort of a local or remote forcing. In the positive IOD, an increase in the wind stress curl occurs in the eastern equatorial region, resulting in decreased SSH and SST but a higher-than-normal Chl. In contrast to that observed in the east, a decrease in the wind stress curl exists in the equatorial south, corresponding to an increase in SSH, which leads to weak Ekman pumping and a decline in Chl. Here, we chose the 2006 fall positive IOD event and 2010 fall negative IOD event to investigate the coupled physics and biology in the system (Figure 12).

3.4 Positive and Negative IOD events

The 2006 positive IOD events are associated with anomalous easterly winds along the equator, strong southeasterly winds in the southern Indian Ocean, and upwelling-favorable alongshore winds off the coast of Sumatra (Figure 12c). Wind stress curl anomalies over the equatorial east are positive and negative over the southern ocean and west of the BoB, as shown in Figure 12a. This finding suggests that the increase in wind-induced Ekman pumping in the east results in lower SSH and play an important role in forming colder SST and higher Chl in both the surface and subsurface. In contrast, an increase in SSH occurs in the south, where negative wind stress curl anomalies are colocated. This suggests reduced open ocean Ekman pumping and upwelling in the south equatorial India Ocean, forming the anomalously high SSH (enhanced SSH) and results in low SCh (Figure 12 upper panels). However, the Chl decline in the surface of the south Indian Ocean is relatively weak and is overwhelmed by the anomalous increase in SChl in the east (Figure 12e). The Chl anomalies at 50 m depth are much larger than their surface counterparts. There is a distinct dipole pattern with negative anomalies (decrease) occurring at the southern equator, while positive anomalies (increase) occur over much of the eastern equatorial region in 2006 (Figure 12g).

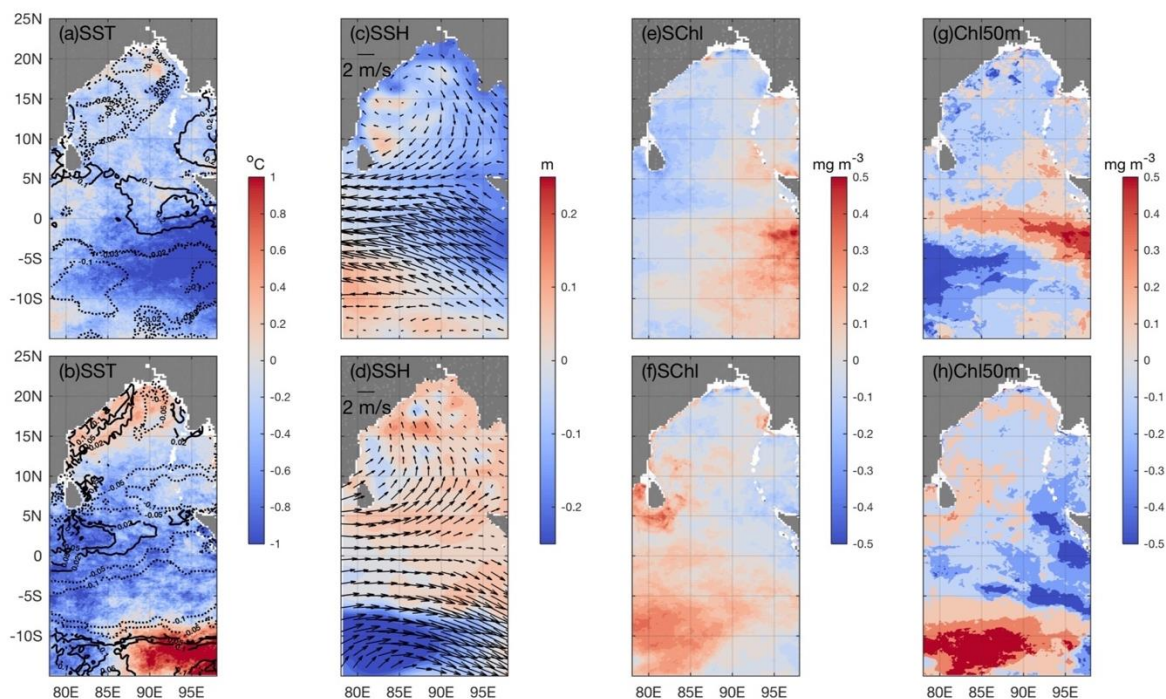


Figure 12. Anomalies with respect to SST, wind stress curl (contour lines in panels a and b), SSH, SChl, and Chl at 50 m depth during 2006 positive IOD events (upper panels) and 2010 negative IOD events (lower panels).

For the fall 2010 negative IOD event, all the variations are opposite to the 2006 positive IOD event (Figure 12 lower panels). However, the prominent SChl increase in the area south of Sri Lanka and along the southern equator at ~5-10°S is notable (Figure 12f), with the same magnitude as the SChl increase in the east during the positive 2006 IOD event. This explains the reason that increase in SChl during fall 2010 in the southern equator from 5-10°S is captured as the first dominant mode by the EOF of the SChl anomaly (Figure 11c).

The subsurface Chl anomalies captured by the vertical Chl field during 2006 positive and 2010 negative IOD events support our prior analysis (Figure 13). The Chl anomalies along 5°S present a dipole pattern with subsurface anomalies that are much larger than their surface counterparts. The positive anomalies in the east during 2006 are accompanied by a shoaling of MLD in the east (shallower compared with the climatology) and deepen in the west (Figure 13a). In the negative IOD event in 2010, the spatial pattern of the anomalies has the opposite sign to that during 2006 (Figure 13b). There are distinct subsurface Chl increases in the west, along with notable Chl increases in the surface mixed layer and relatively weak shallowing of the mixed layer in the west.

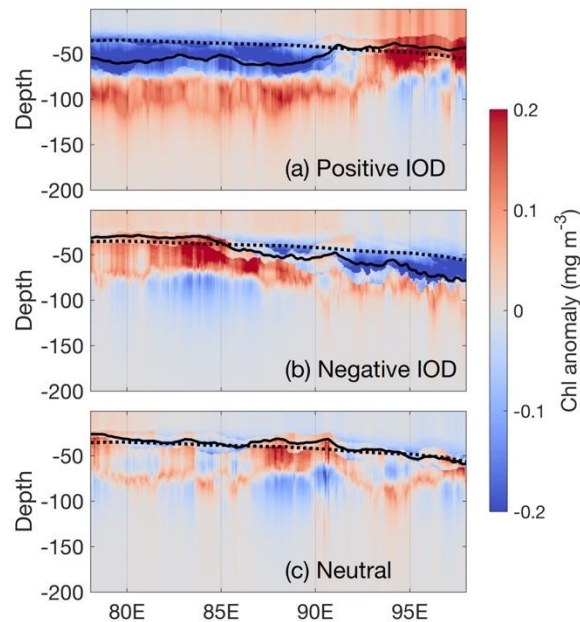


Figure 13. Comparison of Chl and MLD anomalies along section 5°S under three phases of IOD. (a) Positive IOD (2006), (b) Negative IOD (2010), and (c) Neutral year (2009). The black line on each of the plots indicates the MLD depth during that period, and the dashed line indicates the 16-year climatology of MLD along this section.

4 Summary and Discussion

In our analysis, the Chl values used are based on the derivation of different satellite products, numerical modeling for the physical field, and ocean profiles of nitrate to provide information on the nitracline depths to parameterize photoacclimation and nutrient stress. This method is an alternative way to assess the physically induced change in vertical biology under the conditions of limited long-term ecosystem assessments, such as the North Indian Ocean. An analysis of 16-year Chl provides an opportunity to study seasonal cycles as well as interannual variability and ecosystem responses to climatic forcings. Combined with reanalyzed model products of weather and the physical environment in the ocean interior and satellite-based monitoring of SSH, a deeper understanding of the Chl spatiotemporal dynamics and biophysical feedbacks becomes possible.

In this paper, we decompose the Chl variability into principal modes by EOF analysis and statistically identify biota zones with different seasonal/interannual signals. We also document the vertical feature of Chl and link it to the combined effects of monsoonal wind and atmospheric flux, which control vertical mixing. The dominant feature of Chl variability in the BoB is the monsoonal-directed seasonal cycle, in both the surface and subsurface

waters. Summer-time high SChl in the areas west and south of Sri Lanka are associated with summer monsoon-driven coastal upwelling. High SChl values in eastern Sri Lanka, referred to as SLD, are detected annually in the SChl time series. The vertical distribution of Chl indicates that the dome develops along with the MLD lift in the center and results in an enhanced surface Chl concentration. There is evidence of the decay of the dome as it propagates to the north in fall from the time series of SChl along 85°E. However, another hotspot of high SChl occurs in northern Sri Lanka southwest of the BoB. With the monsoon's transition to the northeast mode, dry and strong northeast winds introduce strong mixing in the bay as well as Ekman pumping due to a positive wind stress curl. Wintertime high SChl in the southwest of the BoB are then associated with nutrient intrusion due to Ekman pumping along with increased heat loss. In our analysis, we observe the deepening of the MLD and shallowing of nitracline in the northern part along the 85°E section during fall; however, we cannot separate whether the Ekman pumping-induced nutrient entrainment into the mixed layer or winter convection-driven vertical mixing contributes to the surface Chl increase since either process could contribute to the intrusion of nutrient to the surface and trigger Chl variability. There could also be other top-down control, such as the zooplankton dilution fading effect on the phytoplankton loss due to strong mixing (Behrenfeld, 2010). Therefore, further analyses need to be developed to understand the unique monsoon-driven system.

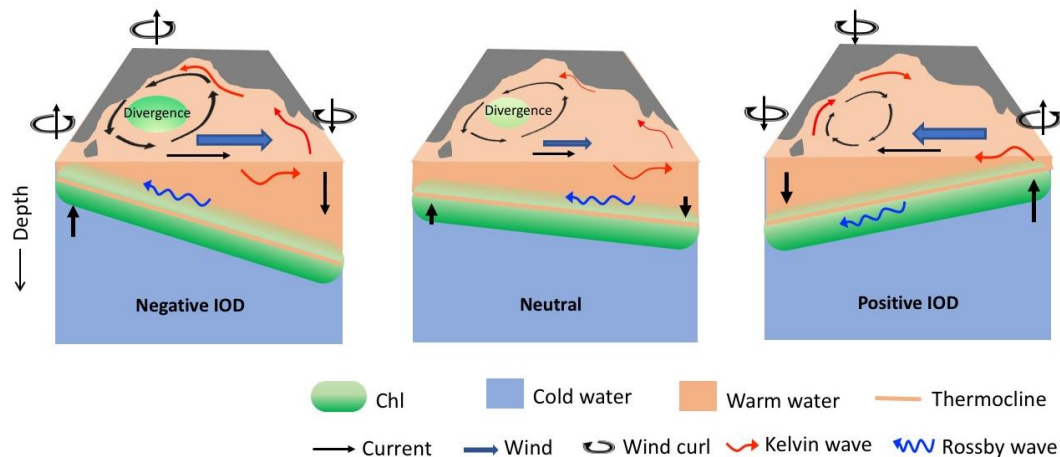


Figure 14. A schematic of the effect of three phases of the IOD mode on ocean physical-biological interactions. The left panel shows the IOD in the positive phase, the middle is in the neutral phase, and the right is in the positive phase.

Interannual SChl anomalies are detected in the southwest BoB with less distinct decline in Chl during the positive IOD event (2006) and significantly enhanced SChl during the negative IOD event (2010). This result could be explained by both the local forcing and remote forcing from the equator. In the positive IOD, there is a negative wind curl over the area west of the BoB, in addition to anomalously strong upwelling Kelvin waves along the equator, which set up strong northward currents along the western boundary and southward currents along the eastern boundary. These currents establish an anticyclonic circulation along the perimeter of the bay that is opposed to the normal cyclonic circulation (Rao, et al., 2002), which counteracts the surface divergence and leads to a decline in Chl in this region. In contrast, in the negative IOD, an enhanced wind curl and anomalously strong cyclonic circulation exist in the bay, which superimpose onto the normal cyclonic circulation and strengthen the Ekman pumping, showing that the biology is enhanced by Chl (Figure 14).

In the equatorial and southern regions, significant interannual variabilities are detected in both the surface and subsurface. The DMI is correlated with interannual anomalies in wind, SSH, and Chl that are derived independently using thermal satellite radiometry, satellite altimetry and model data assimilation. In the IOD event, distinct oscillations were present between the east and southwest in the physical fields; however, they were only apparent in the subsurface Chl from approximately 50 m depth to 80 m depth. One of the reasons for the less dominant dipole pattern in the surface is because the equatorial region in our study site is less productive on the surface due to strong stratification, and a decrease cannot be detected easily in the region with low Chl. Another reason is that compared with subsurfaces in which upwelling/entrainment occur and may properly account for thermocline variability, other mechanisms, such as surface heat exchange and horizontal advection by anomalous currents, could result in a more complicated surface environment, less significantly correlated Chl and a single physical index.

The physical regulations of ocean productivity have focused on nutrient inputs to the mixed layer from deep layers, especially in the oligotrophic tropic ocean. In the Indian Ocean, the change in the equatorial thermocline is unique and is associated with a counteracting (superimposed) effect with neutral IOD conditions in positive (negative) IOD events. Under neutral conditions, the westerly winds blow over the tropical Indian Ocean, and the thermocline is slightly deeper in the east. The positive IODs are associated with a raised thermocline in the east, counteract the climatological west-to-east thermocline gradient, and turn the thermocline gradient to east to west, so only in a strong positive IOD event can such thermocline-induced variability be transmitted to the surface. However, in the negative IOD events, the anomalous westerlies deepen the thermocline in the east and raise it in the west, superimposing it on the neutral west-to-east thermocline. In this condition, the thermocline variability is coupled with the climatological condition, so even a less significant negative IOD event can contribute to interannual anomalies in the magnitude of the surface biological response in the region that has a shallower thermocline (Figure 14). This is the reason why the EOF first dominant mode of the SChl anomaly is confined to the equatorial south with a relatively shallow thermocline (Xie et al., 2002); a modest change in the thermocline depth can significantly change the nutrient distribution and hence impact SChl. Although the ENSO is another important factor that has been determined to have a teleconnection with thermocline feedback in this region (Xie et al., 2002; Yu et al., 2005), how these two interannual climate signals interact with each other and regulate physics and biology needs to be further studied.

This study was based on a variety of datasets to assess the response of Chl to changes in the air forcing, MLD, to gain a better understanding of the physical processes driving the biological patterns in the North Indian Ocean. Proper estimation of the vertical distribution of Chl by CbPM considers the influence of photoacclimation and nutrient stress, which helps to better understand the Chl distributions in the water column, especially in terms of further insight into the consequence of changes in physics to biology under different mechanisms. This result give a general picture of Chl variability in the North Indian Ocean and the equatorial region, will have implications for further accurate estimations of primary production, which is now generally based on Chl, as well as the export of fixed C out of the upper mixed layer by ocean color remote sensing in the unique Indian Ocean under the scenario of climate change.

Acknowledgments

The contributions of Y. Xu were supported by the National Science Foundation of China (Grant No. 41606025). Y. Wu is supported by the National Science Foundation of China (Grant No. 41876074). H.W. Wang is supported by National Science Foundation of China (Grant No. 41606037). We thank Qinseng Wei for providing the cruise Chl data. All datasets used in this study are publicly available online at: https://figshare.com/articles/JGROceans_IO/12236078.

Figure captions

Figure 1. Leading modes of EOF results for SChl. Upper panels show the spatial structures of the first four modes (a)-(d). The temporal amplitudes for the four modes are shown in (e)-(h).

Figure 2. Seasonal climatology of SSH anomalies (color; m), wind stress curl (contour lines; 10^{-6} N m^{-3}), and wind vectors (scale factor is 5 m s^{-1}).

Figure 3. (a) Four biota zones identified by the EOF analysis. (b) Seasonal climatology of spatial mean SChl in the four biota zones. (c) Seasonal climatology of spatial mean SST (solid line) and NHF (dashed line) in the four biota zones.

Figure 4. Time series of vertical Chl in biota zone 1 (a) and zone 2 (b). The black lines represent the euphotic zone depth, and the white lines represent the MLD. Right panel: Comparison of two Chl profiles with one at the time when SChl is highest (solid line) and the other when SChl is lowest (dashed line). (c) is for the grid in zone 1. (d) is for the grid in zone 2.

Figure 5. EOF analysis of Chl in the section along 85°E . (a) Spatial structure of the 1st EOF mode. The EOF of the MLD is overlaid (solid black line), and the climatology of the MLD is overlaid as a black dashed line. (b) Temporal amplitudes of Chl (solid line) and MLD (dashed line). (c) Spatial structures of EOF mode 2 for Chl and MLD. (d) Temporal amplitudes of EOF mode 2 of Chl (solid line) and MLD (dashed line).

Figure 6. Seasonal climatology of MLD (black), nitracline (blue) and NHF (orange) along the section at 85°E .

Figure 7. Time series of SChl along 85°E as a function of latitude and year from 2003-2018. SSH anomalies are plotted as black dashed lines (contour interval 0.1 m). The -0.1 contour lines are highlighted as bold dashed lines.

Figure 8. Time series of vertical Chl in biota zone 3 (a) and zone 4 (b). The black lines represent the euphotic zone depth. The white lines represent MLD. Right panel: Comparison of two Chl profiles with one at the time when SChl is highest (solid line) and the other when SChl is lowest (dashed line). (c) is for the grid in zone 3. (d) is for the grid in zone 4.

Figure 9. EOF analysis of Chl in the section along 5°S . (a) Spatial structure of the 1st EOF mode. The EOF of the MLD is overlaid (solid black line), and the climatology of the MLD is overlain as a black dashed line. (b) Temporal amplitudes of Chl (solid line) and MLD (dashed line). (c) Spatial structures of EOF mode 2 for Chl and MLD. (d) Temporal amplitudes of EOF mode 2 of Chl (solid line) and MLD (dashed line).

Figure 10. Seasonal climatology of MLD (black), nitracline (blue) and NHF (orange) along the section at 5°S .

Figure 11. Spatial structure of the first EOF mode of anomalous wind stress curl (a), SSH (b), SChl (c), and Chl at 50 m (e). The second EOF mode of SChl is plotted in (d). In (a), the EOF modes of the wind component are shown as vectors. The temporal amplitudes are shown in (f) with the DMI. The contour lines in each of the maps indicate the pixel-by-pixel correlation coefficients (passing the 99% significance level) between the DMI and anomalies,

the solid line indicates a positive correlation, and the dashed line indicates a negative correlation.

Figure 12. Anomalies with respect to SST, wind stress curl (contour lines in panels a and b), SSH, SChl, and Chl at 50 m depth during 2006 positive IOD events (upper panels) and 2010 negative IOD events (lower panels).

Figure 13. Comparison of Chl and MLD anomalies along section 5°S under three phases of IOD. (a) Positive IOD (2006), (b) Negative IOD (2010), and (c) Neutral year (2009). The black line on each of the plots indicates the MLD depth during that period, and the dashed line indicates the 16-year climatology of MLD along this section.

Figure 14. A schematic of the effect of three phases of the IOD mode on ocean physical-biological interactions. The left panel shows the IOD in the positive phase, the middle is in the neutral phase, and the right is in the positive phase.

References

- Behrenfeld, M. J., Boss, E., Siegel, D. A., & Shea, D. M. (2005). Carbon-based ocean productivity and phytoplankton physiology from space. *Global Biogeochem. Cycles*, 19, GB1006, doi:10.1029/2004gB002299.
- Behrenfeld, M. J., O'Malley, Robert T., Siegel, D. A., McClain, C. R., Sarmiento, J. L., & Feldman, G. C., et al. (2006). Climate-driven trends in contemporary ocean productivity. *Nature*, 444(7120), 752-755.
- Behrenfeld, M. J. (2010). Abandoning Sverdrup's Critical Depth Hypothesis on phytoplankton blooms. *Ecology*, 91: 977-989. doi:10.1890/09-1207.1
- Brewin, R. J. W., Hirata, T., Hardman-Mountford, N. J., Lavender, S. J., Sathyendranath, S., Barlow, R. (2012). The influence of the Indian Ocean Dipole on interannual variations in phytoplankton size structure as revealed by earth observation. *Deep Sea Research Part II Topical Studies in Oceanography*, 77–80, 117–127.
- Burns, J. M., Subrahmanyam, B., & Murty, V. S. N. (2017). On the dynamics of the Sri Lanka Dome in the Bay of Bengal. *J. Geophys. Res. Oceans*, 122, 7737–7750, doi:10.1002/2017JC012986.
- Chavez, F. P., Messié, Monique, & Pennington, J. T. (2011). Marine primary production in relation to climate variability and change. *Annu. Rev. Mar. Sci.*, 3(1), 227-260.
- Chavez, F. P., Messié, Monique, & Pennington, J. T. (2011). Marine primary production in relation to climate variability and change. *Annu. Rev. Mar. Sci.*, 3(1), 227-260.
- Chen, Gengxin, Han, Weiqing, Li, Yuanlong & Wang, Dongxiao. (2016). Interannual Variability of Equatorial Eastern Indian Ocean Upwelling: Local versus Remote Forcing. *J. Phys. Oceanogr.*, 46. 10.1175/JPO-D-15-0117.1.
- Currie, J., Lengaigne, M., Vialard, J., Kaplan, D., Aumont, O., Maury, O. (2013). Indian Ocean Dipole and El Niño/Southern Oscillation impacts on regional chlorophyll anomalies in the Indian Ocean. *Biogeosciences*, 10, 5841–5888.
- Falkowski, P. G., & Oliver, M. J. (2007). Mix and match: how climate selects phytoplankton. *Nature reviews*, 5(10), 813-819.
- Gregg, W. W. & Watson, W. (2003). Ocean primary production and climate: global decadal changes. *Geophys. Res. Lett.*, 30(15), 1809.
- Gruber, N., Keeling, C. D., & Bates, N. R. (2002). Interannual variability in the North Atlantic Ocean carbon sink. *Science*. 298(5602), 2374–2378, doi:10.1126/science.1077077.
- Huang, B., & Kinter III, J. L. (2002). Interannual variability in the tropical Indian Ocean. *J. Geophys. Res.*, 107(C11), 3199, doi:10.1029/2001JC001278.

- Joseph, S., Wallcraft, A. J., Jensen, T. G., Ravichandran, M., Shenoi, S. S. C., & Nayak, S. (2012). Weakening of spring Wyrki jets in the Indian Ocean during 2006–2011. *J. Geophys. Res.*, 117, C04012, doi:10.1029/2011JC007581.
- Karl, D. M., Christian, J. R., Dore, J. E., Hebel, D. V., Letelier, R. M., Tupas, L. M., & Winn, C. D. (1996). Seasonal and interannual variability in primary production and particle flux at Station ALOHA. *Deep Sea Research Part II*, 43(2–3), 539–568, [https://doi.org/10.1016/0967-0645\(96\)00002-1](https://doi.org/10.1016/0967-0645(96)00002-1).
- Kumar, M. R. R., & Prasad, T. G. (1997). Annual and interannual variation of precipitation over the tropical Indian ocean. *J. Geophys. Res.*, 102(C8), 18,519–18,527.
- Kumar, P. S., Muraleedharan, P. M., Prasad, T. G., Gauns, M., & Madhupratap, M. (2002). Why is the Bay of Bengal less productive during summer compared to the Arabian Sea? *Geophys. Res. Lett.*, 29(24), 2235, doi:10.1029/2002GL016013.
- Lévy, M., Shankar, D., André, J. M., Shenoi, S. S. C., Durand, F., & de Boyer Montégut, C. (2007). Basin-wide seasonal evolution of the Indian Ocean's phytoplankton blooms. *J. Geophys. Res.*, 112(C12). doi:10.1029/2007jc004090.
- Ma, J., Liu, H., Lin, P. & Zhan, H. (2015). Effects of the interannual variability in chlorophyll concentrations on sea surface temperatures in the east tropical Indian Ocean. *J. Geophys. Res. Oceans*, 120, 7015–7027, doi:10.1002/2015JC010862.
- McCreary, J. P., Kundu, P. K., & Molinari, R. L. (1993). A numerical investigation of dynamics, thermodynamics and mixed-layer processes in the Indian Ocean. *Prog. Oceanogr.*, 31, 181–244.
- Murtugudde, R., McCreary, J. P., & Busalacchi, A. J. (2000). Oceanic processes associated with anomalous events in the Indian Ocean with relevance to 1997–1998. *J. Geophys. Res.*, 105, 3295–3306, doi: <https://doi.org/10.1029/1999JC900294>.
- Rao, S. A., Behera, S. K., Masumoto, Y., & Yamagata, T. (2002). Interannual subsurface variability in the tropical Indian Ocean with a special emphasis on the Indian Ocean dipole. *Deep-Sea Research, Part II*, 49, 1549–1572.
- Rao, S. A., & Behera, S. K. (2005). Subsurface influence on SST in the tropical Indian Ocean: Structure and interannual variability. *Dyn. Atmos. Oceans*, 39, 103–135.
- Saji, N. H., Goswami, B. N., Vinayachandran, P. N., & Yamagata, T. (1999). A dipole mode in the tropical Indian Ocean. *Nature*, 401(6751), 360–363.
- Schott, F. A., & McCreary, J. P. (2001). The monsoon circulation of the Indian Ocean. *Prog. Oceanogr.*, 51(1), 1–123.
- Schott, F., Xie, S. P., & McCreary, J. P. (2009). Indian Ocean circulation and climate variability. *Rev. Geophys.*, 47(1), doi: 10.1029/2007RG000245.
- Shetye, S. R., Gouveia, A. D., Shenoi, S. S. C., Sundar, D., Michael, G. S., & Nampoothiri, G. (1993). The western boundary current of the seasonal subtropical gyre in the Bay of Bengal. *J. Geophys. Res.*, 98(C1), 945–954.
- Sverdrup, H. U. (1953). On conditions for the vernal blooming of phytoplankton. *ICES J. Mar. Sci.*, 18(3), 287–295, doi:10.1093/icesjms/18.3.287.
- Thushara, V., Vinayachandran, P. N. M., Matthews, A. J., Webber, B. G. M., & Queste, B. Y. (2018). Vertical distribution of chlorophyll in dynamically distinct regions of the southern Bay of Bengal. *Biogeosciences*, 16, 1447–1468. <https://doi.org/10.5194/bg-16-1447-2019>.
- Vinayachandran, P. N. & Mathew, S. (2003). Phytoplankton bloom in the Bay of Bengal during the northeast monsoon and its intensification by cyclones. *Geophys. Res. Lett.*, 30, 1572, <https://doi.org/10.1029/2002GL016717>.
- Vinayachandran, P. N., & Yamagata, T. (1998) Monsoon Response of the Sea around Sri Lanka: Generation of Thermal Domes and Anti-cyclonic Vortices. *J. Phys. Oceanogr.*, 28, 1946–1960, 1998.

- Vinayachandran, P. N., Chauhan, P., Mohan, M., & Nayak, S. (2004). Biological response of the sea around Sri Lanka to summer monsoon. *J. Geophys. Res.*, 31, L01302, <https://doi.org/10.1029/2003GL018533>, 2004.
- Vinayachandran, P. N., Murty, V. S. N., & Ramesh Babu, V. (2002). Observations of barrier layer formation in the Bay of Bengal during summer monsoon. *J. Geophys. Res.*, 107(C12), 8018, doi:10.1029/2001JC000831.
- Webster, P. J., Moore, A. M., Loschnigg, J. P., & Leben, R. R. (1999). Coupled ocean–atmosphere dynamics in the Indian Ocean during 1997–98. *Nature*, 401(6751), 356–360.
- Weller, R., Farrar, J., Seo, H., Prend, C., Sengupta, D., Sree Lekha, J., Ravichandran, M., & Venkatesen, R. (2018). Moored observations of the surface meteorology and air-sea fluxes in the northern Bay of Bengal in 2015. *J. Clim.*, 32, 549–573.
- Westberry, T., Behrenfeld, M. J., Siegel, D. A., & Boss, E. (2008). Carbon-based primary productivity modeling with vertically resolved photoacclimation. *Global Biogeochem. Cycles*, 22(2), GB2024, doi:10.1029/2007GB003078.
- Wiggert, J. D., Vialard, J. & Behrenfeld, M. J. (2013). Basin-Wide Modification of Dynamical and Biogeochemical Processes by the Positive Phase of the Indian Ocean Dipole During the SeaWiFS Era. In *Indian Ocean Biogeochemical Processes and Ecological Variability* (eds J.D. Wiggert, R. R. Hood, S. A. Naqvi, K.H. Brink and S. L. Smith). doi:10.1029/2008GM000776.
- Wyrtki, K. (1973). An equatorial jet in the Indian Ocean. *Science*, 181, 262–264.
- Yu, W., Xiang, B., Liu, L., & Liu, N. (2005). Understanding the origins of interannual thermocline variations in the tropical Indian Ocean. *Geophys. Res. Lett.*, 32, L24706, doi:10.1029/2005GL024327.
- Xie, S. P., Annamalai, H., Schott, F. A., McCreary, J. P. (2002). Structure and mechanisms of south Indian climate variability. *J. Clim.*, 9, 840–858.
- Xue, L., Yu, W., Wang, H., Jiang, L. Q., Feng, L., Gao, L., Li, K., Li, Z., Wei, Q., & Ning, C. (2014). Temporal changes in surface partial pressure of carbon dioxide and carbonate saturation state in the eastern equatorial Indian Ocean during the 1962–2012 period. *Biogeosciences*, 11(22), 6293–6305.

Figure 1.

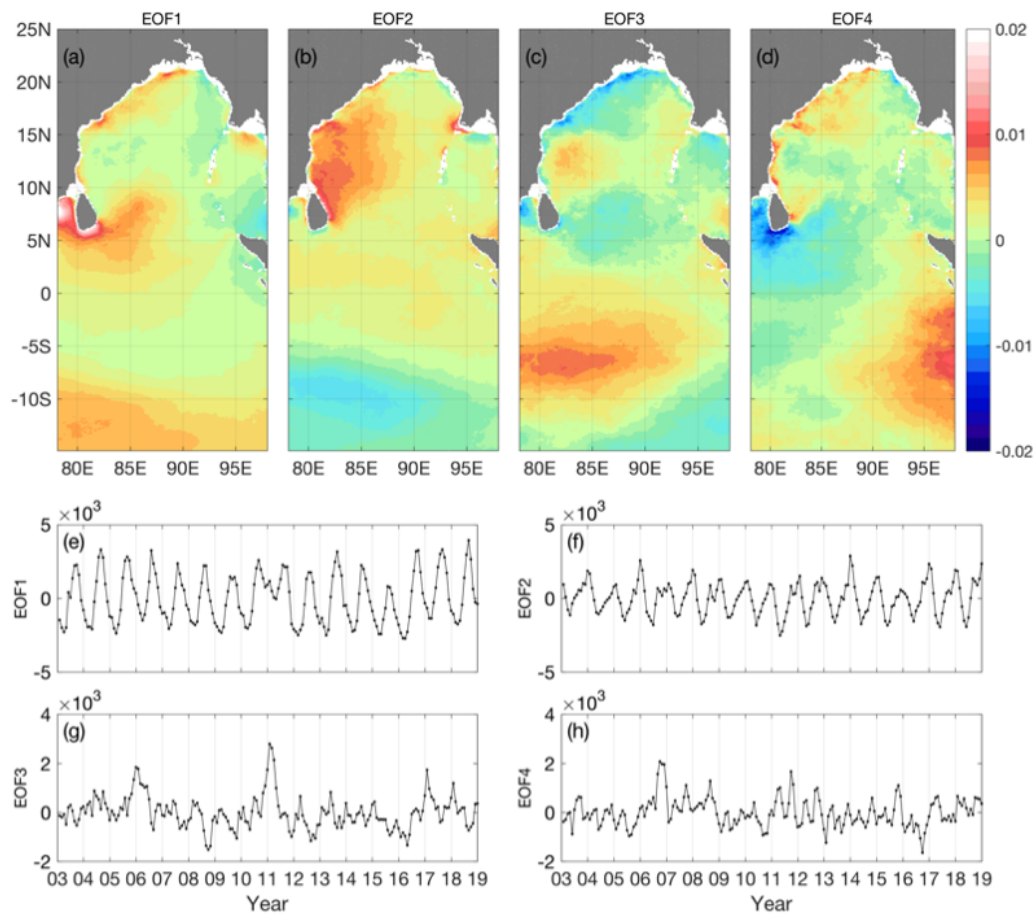


Figure 2.

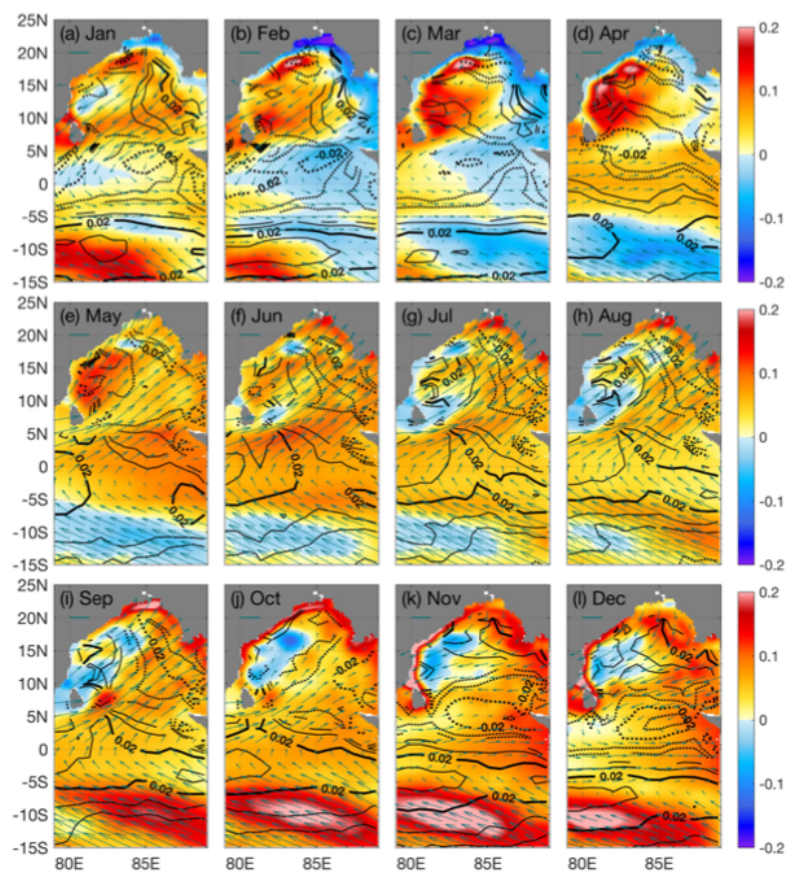


Figure 3.

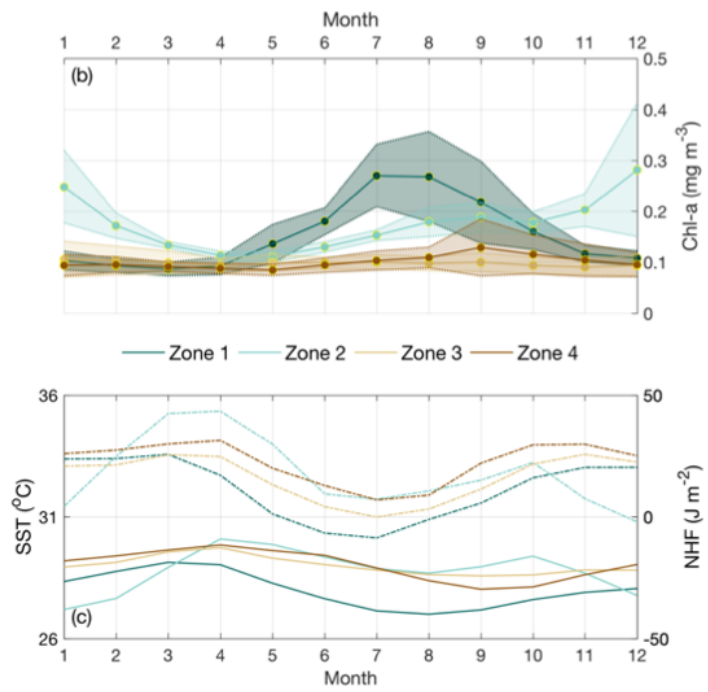
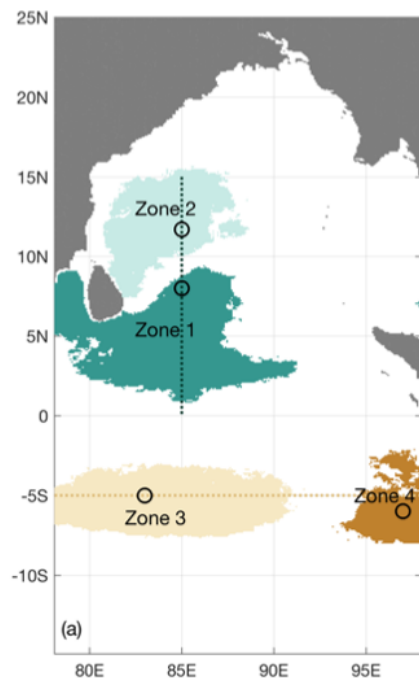


Figure 4.

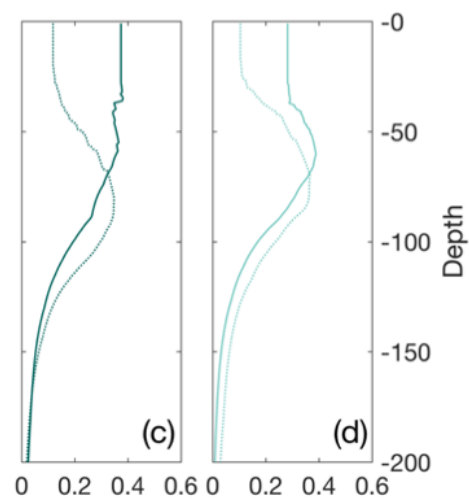
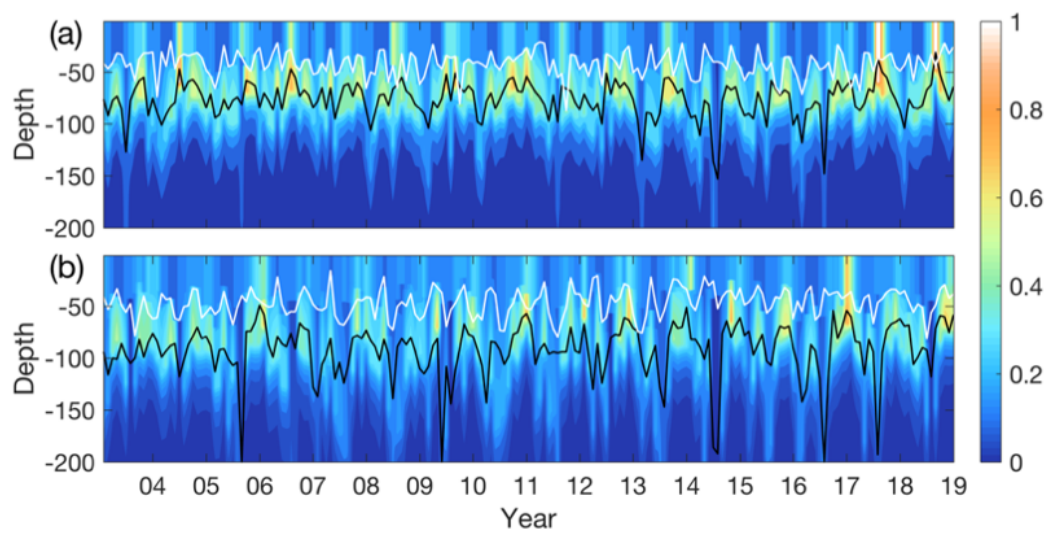


Figure 5.

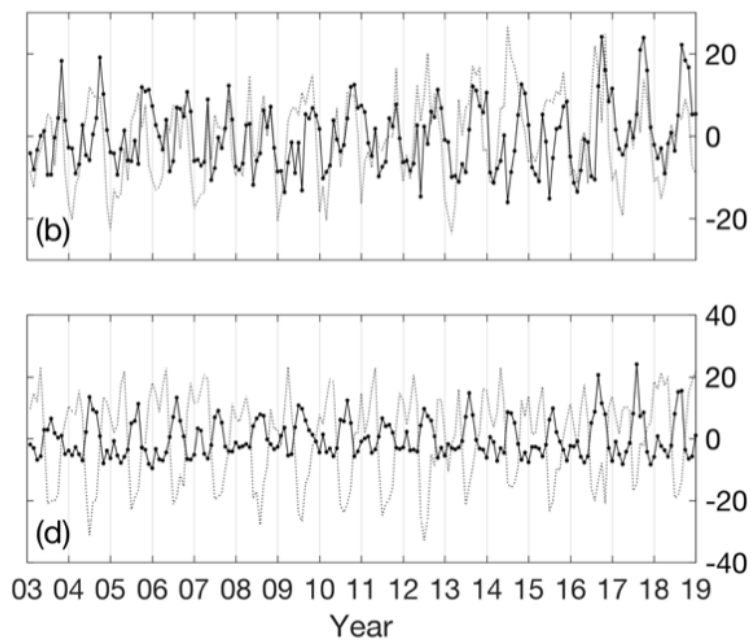
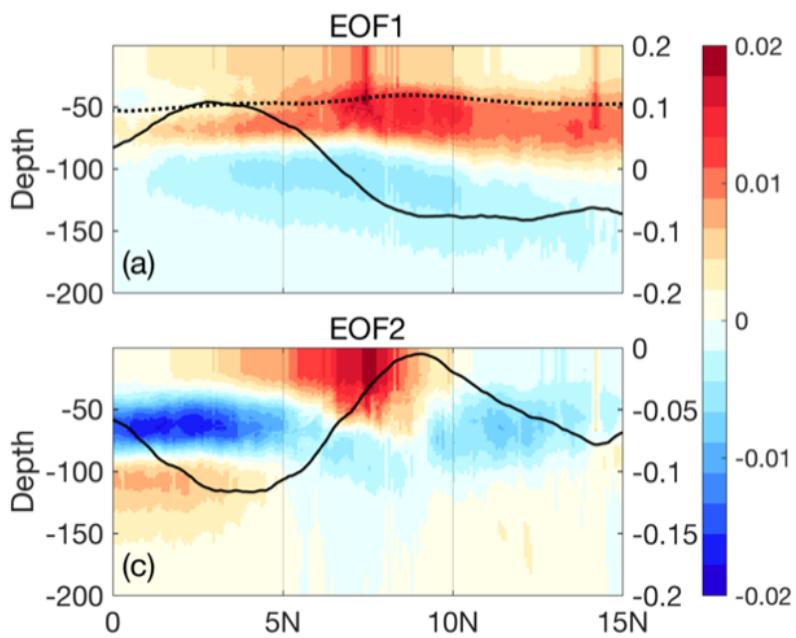


Figure 6.

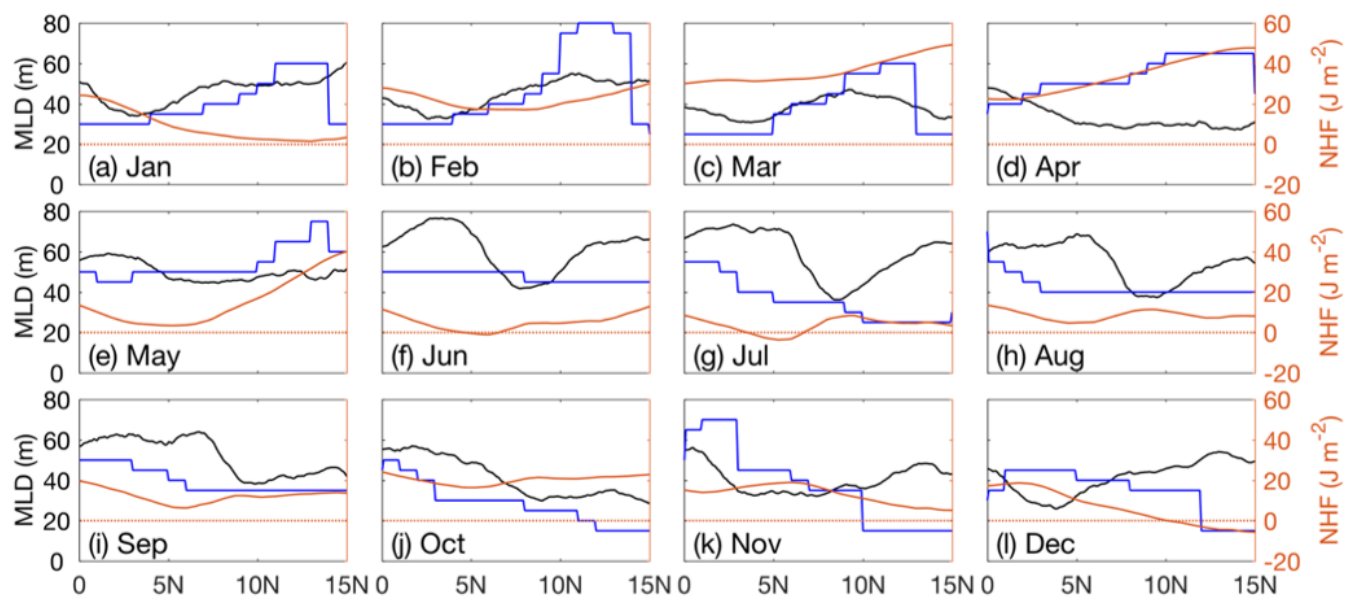


Figure 7.

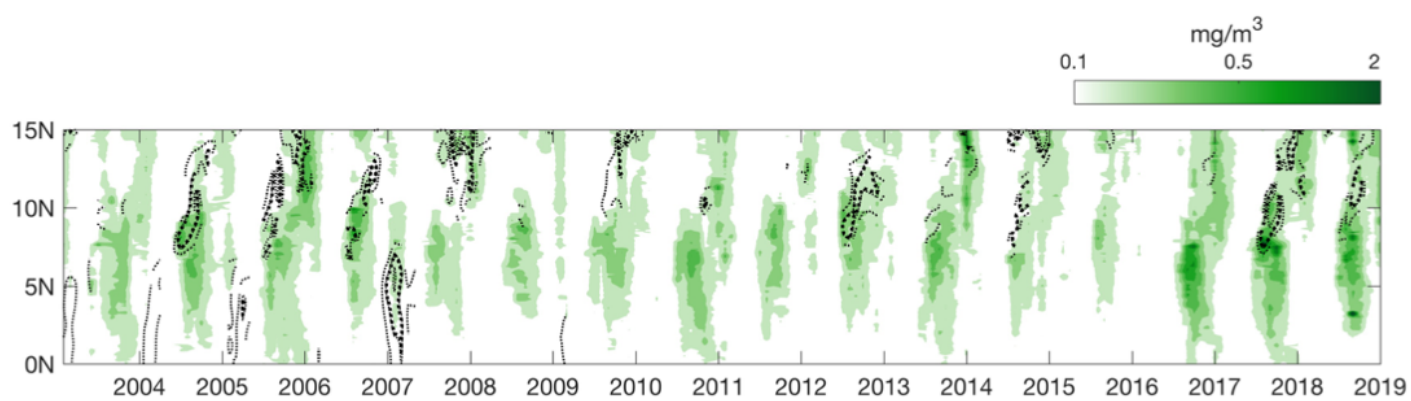


Figure 8.

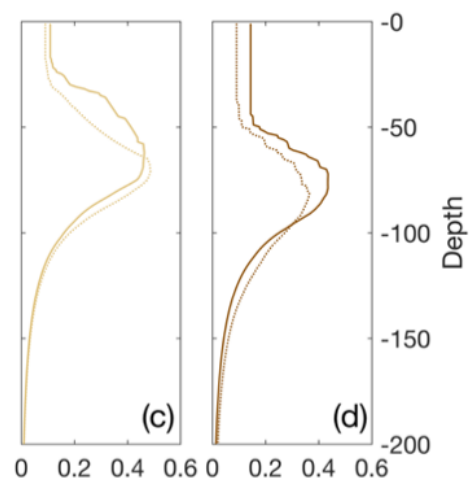
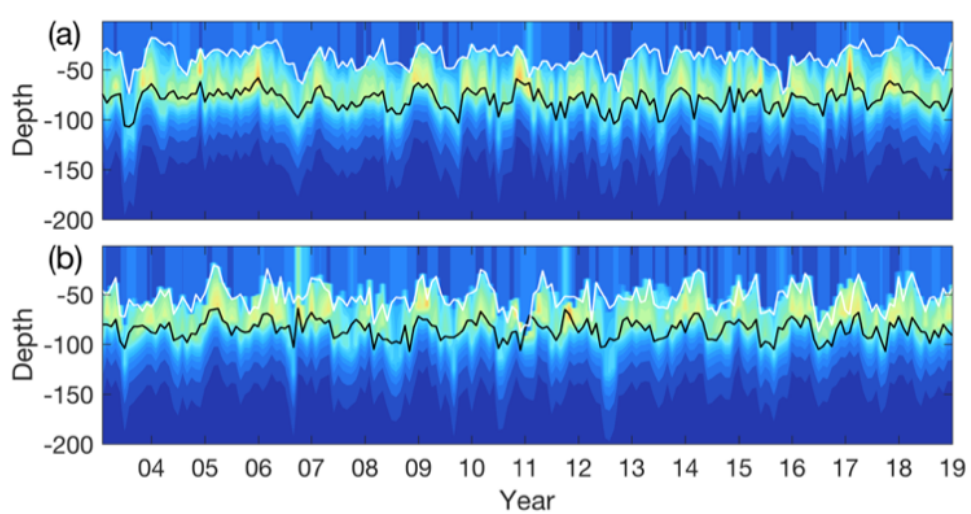


Figure 9.

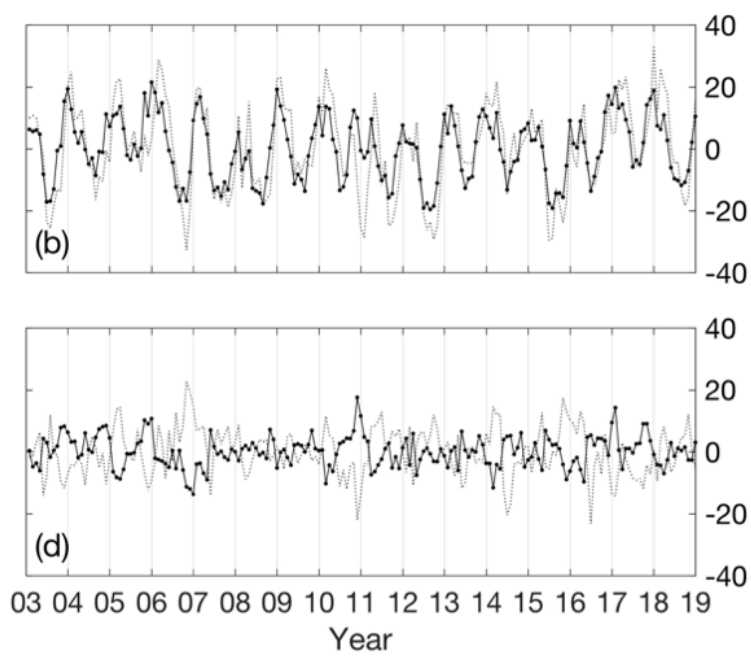
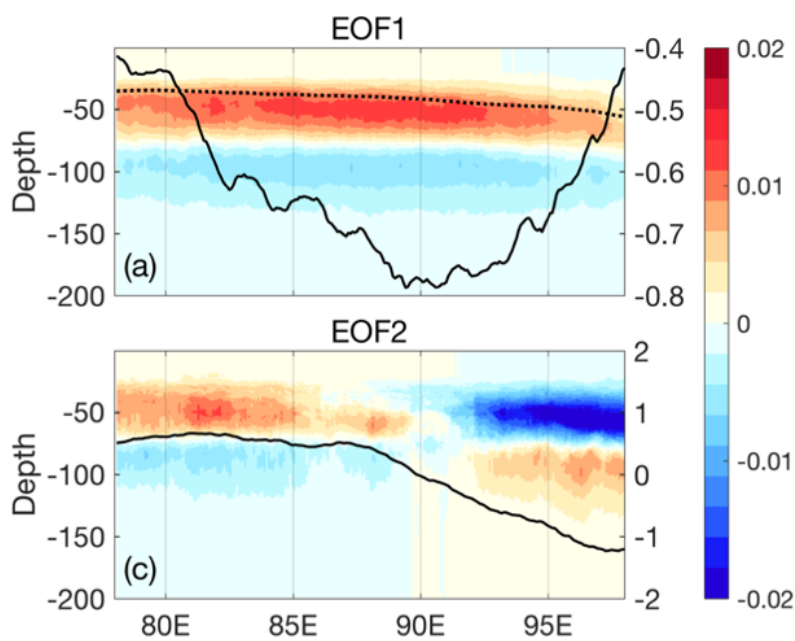


Figure 10.

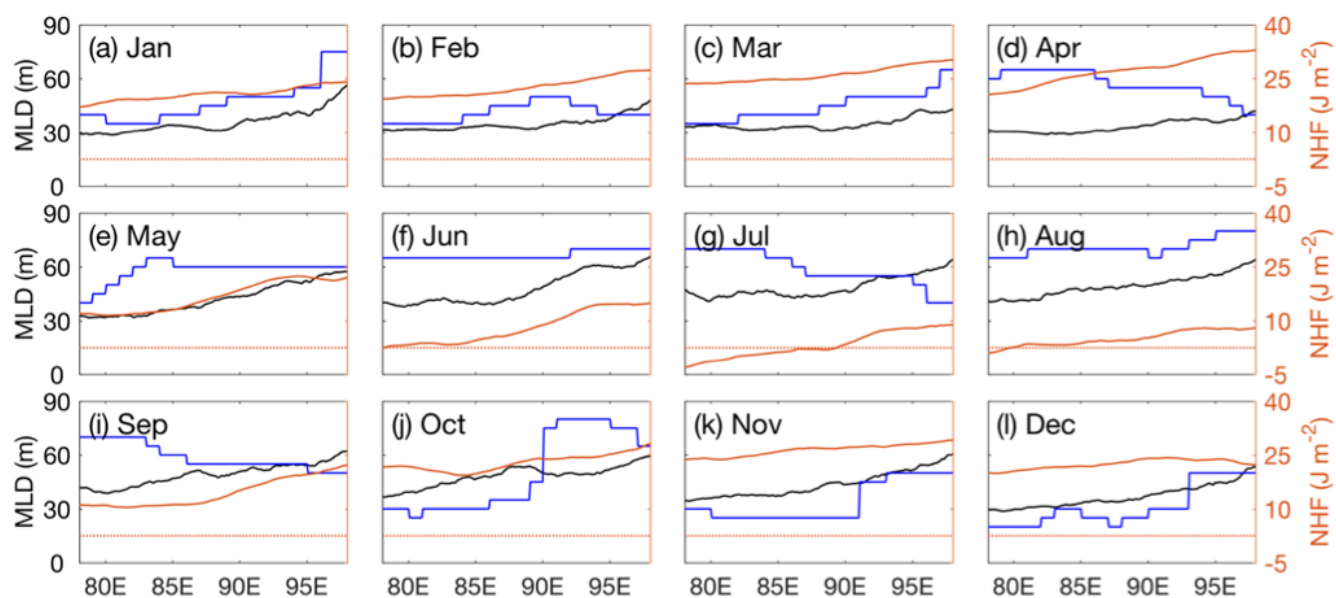


Figure 11.

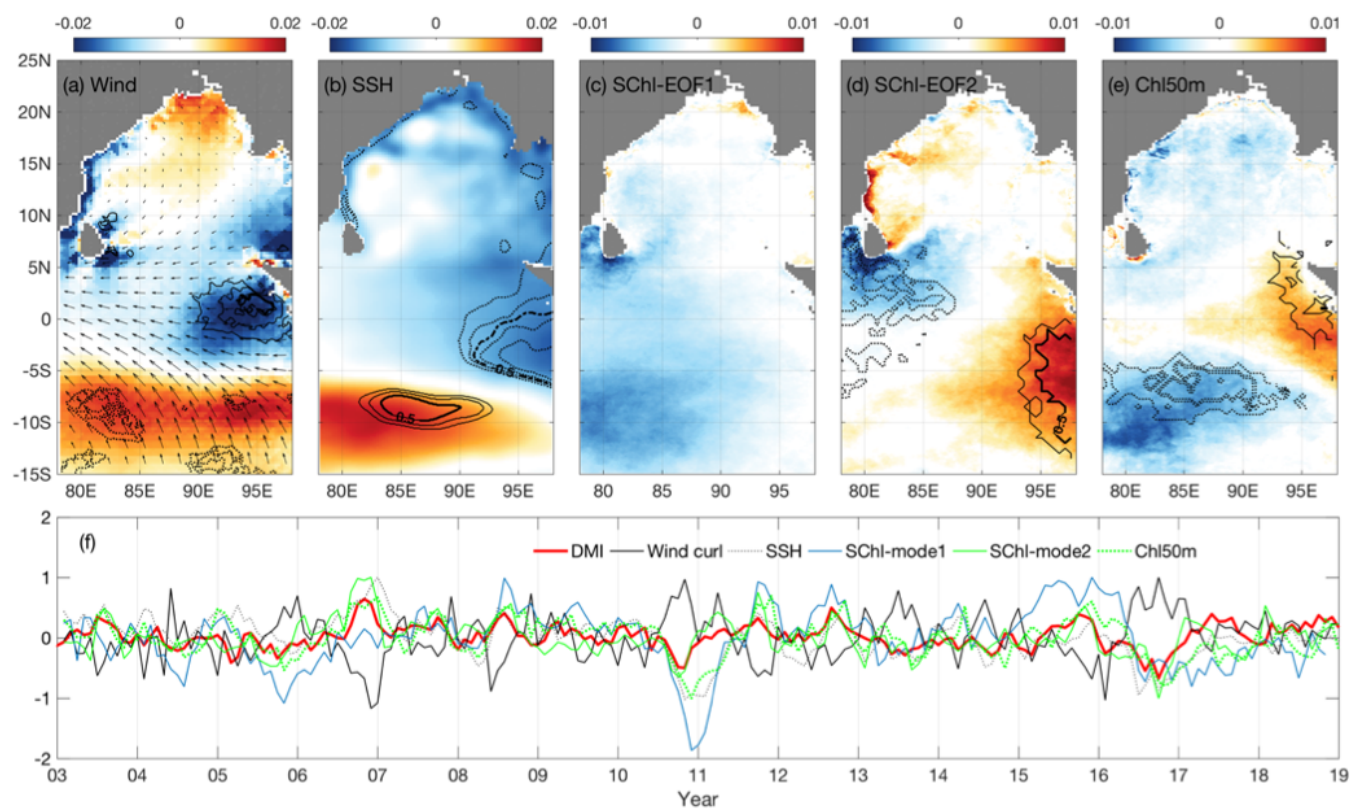


Figure 12.

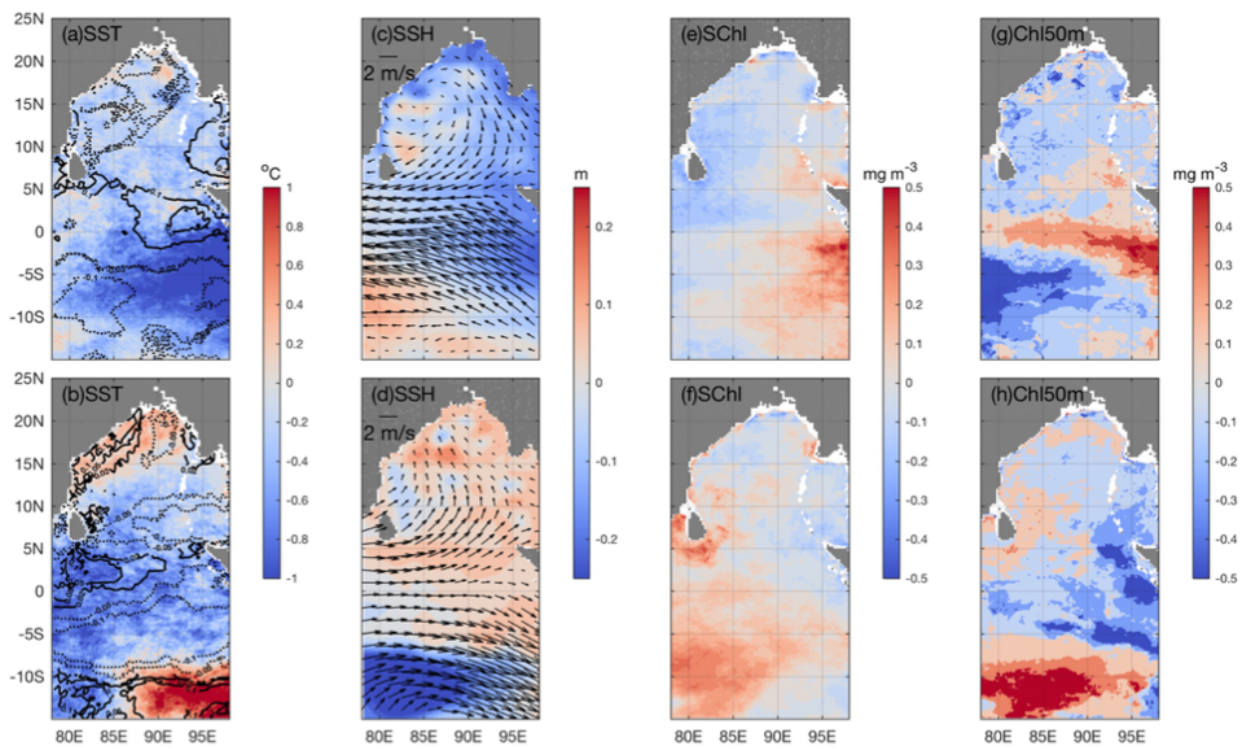


Figure 13.

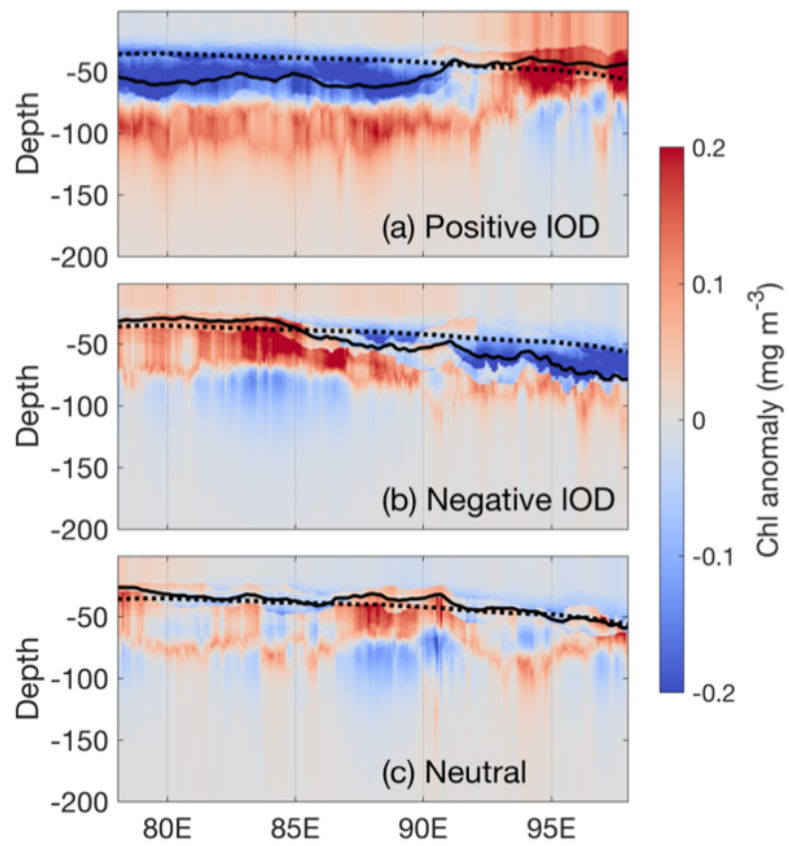


Figure 14.

